Title
Chapter 3: Understanding the Effects of Composition and Structure on the Oxygen Evolution Reaction (OER) Occurring on NiFeOx Catalysts

ISBN
9781782625551

Author
Bell, AT

Publication Date
2019

DOI
10.1039/9781788010313-00079

Peer reviewed

Electrocatalysis

CHAPTER 3

Understanding the Effects of Composition and Structure on the Oxygen Evolution Reaction (OER) Occurring on $NiFeO_x$ Catalysts

ALEXIS T. BELL[a,b]

[a] Joint Center for Artificial Photosynthesis, Lawrence Berkeley National Laboratory, Berkeley, CA 94720, USA; [b] Department of Chemical and Biomolecular Engineering, University of California, Berkeley, CA 94720-1462, USA
Email: alexbell@berkeley.edu

3.1 Introduction

The use of wind and solar energy to carry out the electrochemical splitting of water is a subject of considerable contemporary interest, since hydrogen produced by this means could be used to store renewable but intermittent electrical energy, to power fuel-cell vehicles, and to hydrodeoxygenate biomass or reduce CO_2 to carbon-containing fuels.[1–5] The challenge, therefore, is to develop energy-efficient systems utilizing renewable sources of electricity to achieve the electrochemical splitting of water. This chapter reviews the catalyst requirements for achieving this goal using earth-abundant elements. Particular attention is devoted to oxygen evolution, which occurs

Energy and Environment Series No. 22
Integrated Solar Fuel Generators
Edited by Ian D. Sharp, Harry A. Atwater and Hans-Joachim Lewerenz

Published by the Royal Society of Chemistry, www.rsc.org

at the electrolyzer anode, since this reaction requires a potential well above the minimum set by thermodynamics. We begin by summarizing the thermodynamics for the electrochemical splitting of water and then review what is known about catalysts based on earth-abundant elements that can be used to promote the oxygen evolution reaction. This overview will show that the most promising catalysts are based on oxides and oxyhdroxides containing Ni and Fe. We will next examine in some detail how Fe^{3+} cations incorporate into Ni oxyhydroxides (NiOOH) and what the role of these cations is in promoting the OER. The chapter will end with an examination of recent efforts to find additive elements other than Fe that could be used to enhance the activity of NiOOH and elements that might be added to $Ni_{1-x}Fe_xOOH$ to further enhance its activity.

3.2 Thermodynamics of Water Splitting

The thermodynamic potential for the electrochemical splitting of water, $2H_2O(l) \rightarrow 2H_2(g) + O_2(g)$, is $E_o = -1.23$ V. This overall reaction is comprised of two half reactions, which differ depending on the pH of the electrolyte in which the reaction is carried out. Scheme 3.1 shows the two half reactions and the associated thermodynamic potentials for the extremes of pH = 0 (acid) and pH = 14 (base). Under acidic conditions, water is oxidized at the anode to produce gaseous O_2, protons, and electrons and protons and electrons are recombined at the cathode to produce gaseous H_2. Under basic conditions, hydroxyl anions are oxidized at the anode to produce O_2, water, and electrons and water and electrons react at the cathode to produce gaseous H_2 and hydroxyl anions. The two half reactions are referred to as the oxygen evolution reaction (OER) and the hydrogen evolution reaction (HER).

In Scheme 3.1, the potential (E) for each reaction at pH = 0 is the same as the standard potential (E^0) which is defined for this pH, assuming that the value of E^0 for the HER is 0.00 V. The potential for each half reaction depends on the Nernst equation, which at unit partial pressure of H_2 and O_2 is given by $E_{HER} = -0.59 \times pH$ V for the HER and $E_{OER} = 1.23 - 0.59 \times pH$ V for

In aqueous acid (pH = 0)

$2\ H_2O(l)$	$\rightarrow O_2(g) + 4\ H^+ + 4\ e^-$	$E = E^0 = 1.23$ V
$4\ H^+ + 4\ e^-$	$\rightarrow 2\ H_2(g)$	$E = E^0 = 0.00$ V
$2\ H_2O(l)$	$\rightarrow O_2(g) + 2\ H_2(g)$	$E = E^0 = 1.23$ V

In aqueous base (pH = 14)

$4\ OH^-$	$\rightarrow O_2(g) + 2\ H_2O(l) + 4\ e^-$	$E = 0.40$ V
$4\ H_2O(l) + 4\ e^-$	$\rightarrow 2\ H_2(g) + 4\ OH^-$	$E = -0.83$ V
$2\ H_2O(l)$	$\rightarrow O_2(g) + 2\ H_2(g)$	$E = E^0 = 1.23$ V

Scheme 3.1 Water-splitting half reactions in aqueous acid and base.

the OER. Since the pH at which experiments are carried out differ from experimenter to experimenter, it is convenient to refer potentials to the reversible hydrogen electrode (RHE). Accordingly, E_{OER} *vs.* the RHE (or simply E_{OER} *vs.* RHE) is always 1.23 V.

Regardless of pH, the actual potential required to split water is higher due to reaction barriers associated with the catalysts used at the anode and cathode. This excess potential, known as the overpotential, is a function of the current density passed through the electrolyzer. Since the overpotential increases with increasing current density, the performance of different catalysts must compared at a fixed current density, which is often taken to be 10 mA cm^{-2} and is based on the superficial area of the anode. The overpotentials for the OER and HER are symbolized by η_{OER} and η_{HER}, respectively. The dependence of η_{OER} and η_{HER} on the current density (j) is given by the Tafel equation, $d\eta_{OER}/d\ln(j) = \beta$, where β is referred to as the Tafel slope. This equation and its role in describing the activity of OER catalysts is discussed in greater detail below.

Extensive research has shown that while the overpotential required to drive the cathode reaction (the HER) at 10 mA cm^{-2} can be as low as 50 mV, the overpotential required to drive the anode reaction (the OER) typically exceeds 300 mV.[3,5] The overpotentials for the OER and HER affect the efficiency of water splitting for a given current density, which is defined as the ratio of the thermodynamic potential for water splitting, E_o, divided by the sum of E_o and the overpotentials for the anode and cathode, η_{OER} and η_{HER}, respectively. For example, if $\eta_{HER} = 50$ mV and $\eta_{OER} = 300$ mV, the efficiency for water splitting at 10 mA cm^{-2} (neglecting ohmic and Nernstian losses) would be 78%. Since η_{OER} is significantly larger than η_{HER}, most research in the field of catalysis for water splitting has focused on the discovery and development of catalysts having a low value of η_{OER}, as well as understanding how the chemical composition and structure affect the magnitude of this parameter. It should be noted, though, that comparison of different OER catalysts solely on the basis of the value of η_{OER} at a fixed anodic current density can be misleading, particularly when catalysts are prepared in radically different ways. This topic and the dependence of η_{OER} on current density are discussed at a later point in this chapter.

3.3 Catalysts for the OER

A number reviews, as well as the Chapter 5 by McCrory within this book, have been published concerning catalysts that can be used to promote the OER under both acidic and basic conditions.[3,5–11] These publications show that with the exception of IrO_2 and RuO_2 all of the materials examined are unstable in acid electrolytes, but that there are a large number of metal oxides that are stable in base electrolytes. To illustrate this latter point, Figure 3.1 shows the results of a recent benchmarking study of OER catalysts carried out in 1 M NaOH and with a current density of 10 mA cm^{-2}.[8] It is evident from this figure that the OER catalysts exhibiting the lowest values of

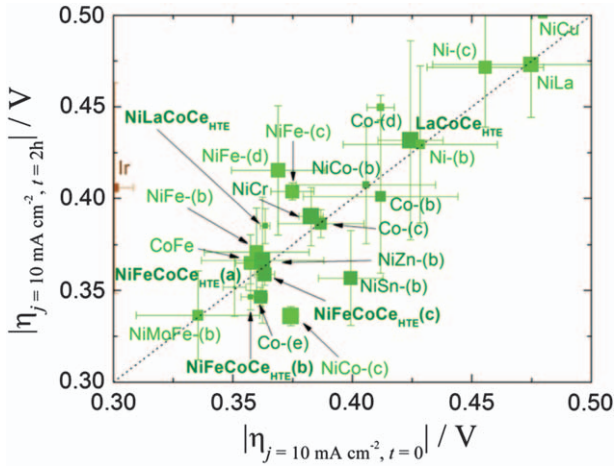

Figure 3.1 Values of η_{OER} determined using a rotating disk electrode in 1 M NaOH. The *x*-axis is the overpotential required to achieve 10 mA cm^{-2} per geometric area at time $t = 0$. The *y*-axis is the overpotential required to achieve 10 mA cm^{-2} per geometric area at time $t = 2$ h. The diagonal dashed line is the expected response for a stable catalyst that does not change in activity during 2 h constant polarization. The color of each point represents the roughness factor of the catalyst with a bin size of 1 order of magnitude with light green representing RF = 1, and dark red representing RF > 104. The size of each point is inversely proportional to the standard deviation in the ECSA measurements. The region of interest for benchmarking is the unshaded white region of the plot where the overpotential required to achieve 10 mA cm^{-2} per geometric area at time $t = 0$ and $t = 2$ h is less than 0.55 V. There is a break and change in scale in both axes at overpotentials >0.55 V, and the corresponding region of the plot is shown in gray. Catalysts whose activity and stability measurements fall inside this gray area are outside the region of interest for benchmarking, but their activity and stability measurements are included for completeness.
Adapted with permission from C. C. L. McCrory, S. Jung, I. M. Ferrer, S. M. Chatman, J. C. Peters and J. F. Jaramillo, Benchmarking Hydrogen Evolving and Oxygen Evolving Reaction Electrocatalysts for Solar Water Splitting Devices, *J. Am. Chem. Soc.* 2015, **137**, 4347–4357, Copyright 2015 American Chemical Society.[8]

η_{OER} are IrO_2 and mixed oxides based on Ni and Fe. It should be noted, though, that while IrO_2 is stable in an acid electrolyte, it loses activity with time. Further details concerning the performance and stability of metal oxide catalysts that operate in acidic and basic electrolytes can be found in Chapter 5 of this book.

Since Fe and Ni are earth-abundant elements, whereas Ir and Ru are among the least earth-abundant and most expensive elements, a great deal of attention has been devoted to understanding why oxides containing Fe and Ni exhibit a low value of η_{OER} and whether the overpotential of such oxides might be reduced further by addition of other elements. For these

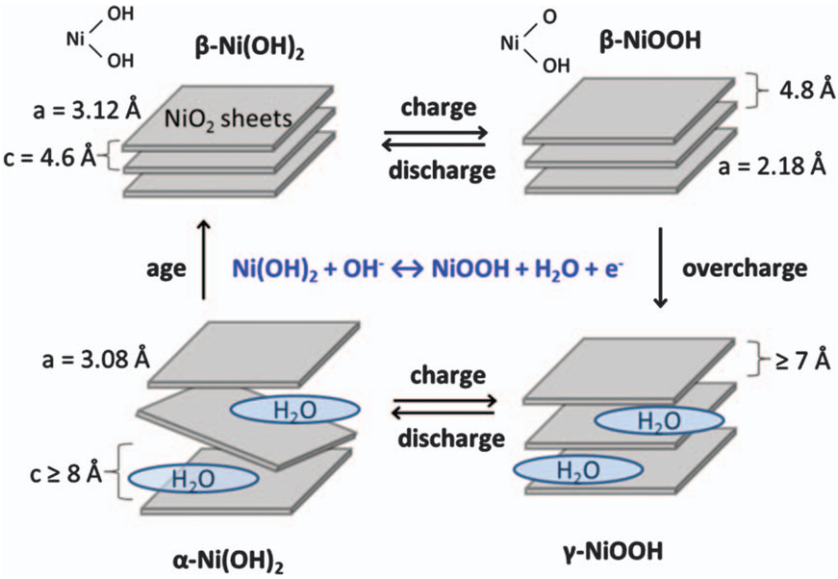

Figure 3.2 Bode scheme for the $Ni(OH)_2$/NiOOH redox transformation. The transformation of β-NIOOH to γ-NiOOH is observed when β-NiOOH is operated at a high OER overpotential for an extended period. This step is referred to as overcharging.

reasons, the balance of this chapter will focus on understanding OER catalysts based on Fe and Ni oxides operated in alkaline media.

An appropriate place to start the discussion of $NiFeO_x$ OER catalysts is by considering what is known about the OER over NiO_x. Identification of Ni oxide as an active catalyst for the OER under alkaline conditions was first reported by Bode in 1966,[12] who noted that the performance of NiO_x depends on the manner in which it is aged. At potentials well below the onset of the OER in KOH solution, the catalyst is present as either α- or β-$Ni(OH)_2$, and prior to the onset of oxygen evolution, this phase oxidizes to form either the β or γ phase of NiOOH *via* the reaction $Ni(OH)_2 + OH^- \rightarrow NiOOH + H_2O + e^-$. The phase of NiOOH depends on the manner of catalyst charging and discharging, as shown in Figure 3.2. Bode also noted that the β phase of NiOOH is more active for the OER than the γ phase. Subsequent studies by various authors have confirmed that the OER activity of NiOOH can be increased by transforming the γ-NiOOH to β-NiOOH phase as a consequence of aging.[13–18] Contemporaneous studies also showed that the OER activity of NiOOH could be enhanced through the addition of Fe.[19–29]

It is important to note, though, that it was not until the work of Boettcher and coworkers,[30] which appeared in 2014, that the increase in OER activity observed with the aging of NiO_x in KOH was recognized to be a consequence of the incorporation of Fe impurities and not due to the transition of γ-NiOOH to β-NiOOH, as had been concluded in earlier studies. These

authors also showed that Fe-free NiOOH is quite inactive for the OER, and exhibits an overpotential in excess of 500 mV at 10 mA cm^{-2}. These findings suggest that virtually all of the earlier studies of the OER on NiO_x were performed with unknown amounts of Fe incorporated into the catalyst.

Isolation of the effects of Fe incorporation from the effects of aging in Fe-free electrolyte on the structure-activity of NiOOH has been reported by Bell and coworkers.[31] $Ni(OH)_2$ films aged in unpurified electrolyte were found to incorporate ≥20% Fe after five weeks of aging in KOH containing <1 ppm of Fe and were $>10^2$ more active than Fe-free films. Films aged in Fe-free electrolyte were predominantly disordered β-$Ni(OH)_2$/β-NiOOH if maintained below 0.7 V *vs.* Hg/HgO (0.84 V *vs.* RHE) in 1 M KOH and 'over-charged' to form a mixture of γ- and β-NiOOH above this potential. Fe-containing $Ni(OH)_2$ films formed β-$Ni(OH)_2$ to a lesser extent and instead exhibited NiOOH structural changes in accordance with the formation of a NiFe-layered double hydroxide phase.

Figure 3.3 illustrates the variation in both the η_{OER} at 10 mA cm^{-2} and the current density for $\eta_{OER} = 300$ mV as a function of the Fe content of the catalyst.[31] As the Fe content increases, the value of η_{OER} decreases from a value of 530 mV in the absence of Fe to a minimum of 280 mV for an Fe content of ~11%. Over the same range of Fe content, the current density at $\eta_{OER} = 300$ mV increases from 0.12 to 20 mA cm^{-2}.

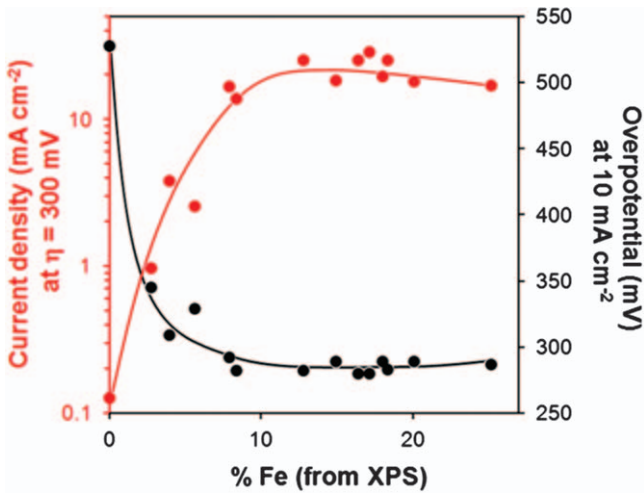

Figure 3.3 Oxygen evolution activity of electrodeposited NiOOH films deposited on Au rotating disk electrodes (RDEs) at 300 mV overpotential and 10 mA cm^{-2} geometric current density in 1 M KOH as a function of Fe content incorporated from the electrolyte. Curves are included to guide the eye.
Reprinted with permission from S. Klaus, Y. Cai, M. W. Louie, L. Trotochaud and A. T. Bell, Effects of Fe Electrolyte Impurities on $Ni(OH)_2$/NiOOH Structure and Oxygen Evolution Activity, *J. Phys. Chem. C,* 2015, **119**, 7243–7254, Copyright 2015 American Chemical Society.[31]

The pattern of activity seen in Figure 3.3 is also observed for electrodeposited and sputtered films of Ni and Fe, as shown in Figure 3.4.[32] In this instance the value of η_{OER} NiOOH is >700 mV and that of FeOOH is ~ 500 mV. The minimum value of η_{OER} is 320 mV and occurs for an Fe content of 20%. It is notable that for the same film thickness, the value of η_{OER} is independent of the manner of film deposition. What is significant, though, is that the values of η_{OER} for NiOOH and FeOOH, as well as the minimum value of η_{OER} and the Fe content at which this occurs are functions of film thickness and extent of Fe and Ni mixing during film deposition. Figure 3.4 also shows that independent of the manner of film deposition, the current density measured at $\eta_{OER} = 300$ mV increases by roughly three orders of magnitude with the addition of even a very small amount of Fe to NiOOH, reaching a maximum current density of ~3 mA cm^{-2} for an Fe content of 20% and then slowly decreasing by nearly three orders of magnitude with the addition of more Fe. The Tafel slope is also a strong function of Fe content. It is 120 mV per dec for pure NiOOH, decreases rapidly to 40 mV per dec with the addition of a small amount of Fe, stays at this value until the Fe content reaches 65%, and then increases to 62 mV per dec for pure FeOOH.

Swierk *et al.* have reported that the Fe content in $Ni_{1-x}Fe_xOOH$ films influences their impedance and apparent activation energy for the OER, in addition to influencing the OER overpotential and Tafel slope.[33] As Fe is incorporated into the NiOOH lattice, the Faradaic resistance associated with the OER decreases and charge relaxation becomes more favorable. These results suggest that the formation of charged surface intermediates is the dominant process for the OER on these films. The activation energy measurements reveal that while isolated Fe-sites in NiOOH lattices have similar energetics regardless of film composition, the overall OER activity is also controlled by structural considerations. Correspondingly, the apparent activation energy for the OER is 76 ± 5 kJ mol^{-1} for pure NiOOH and 66 ± 5 kJ mol^{-1} for pure FeOOH, but decreases to a minimum of ~25 kJ mol^{-1} for $Ni_{0.8}Fe_{0.2}OOH$.

To summarize, recent studies have established that Fe-free NiOOH is not an active OER catalyst but becomes progressively more active with the incorporation of Fe. Therefore, the important questions to address next are what is the structure of $NiFeO_x$ catalysts, what is the nature of the OER-active site (*i.e.*, Fe *vs.* Ni), and what are the effects of preparation on the OER activity of $NiFeO_x$ catalysts?

3.4 The Structure of $FeNiO_x$

Raman and X-ray absorption spectroscopy have been used to characterize the structure of $FeNiO_x$ catalysts as a function of applied potential. Bell and coworkers have reported that a Ni film immersed in 1 M KOH immediately transforms to $Ni(OH)_2$ in the absence of an applied potential.[15,16] Figure 3.5 shows that as the potential is raised from 0 to 1.5 V *vs.* RHE, the spectrum changes from that of $Ni(OH)_2$ (bands at 449 cm^{-1} and 494 cm^{-1}) to that of

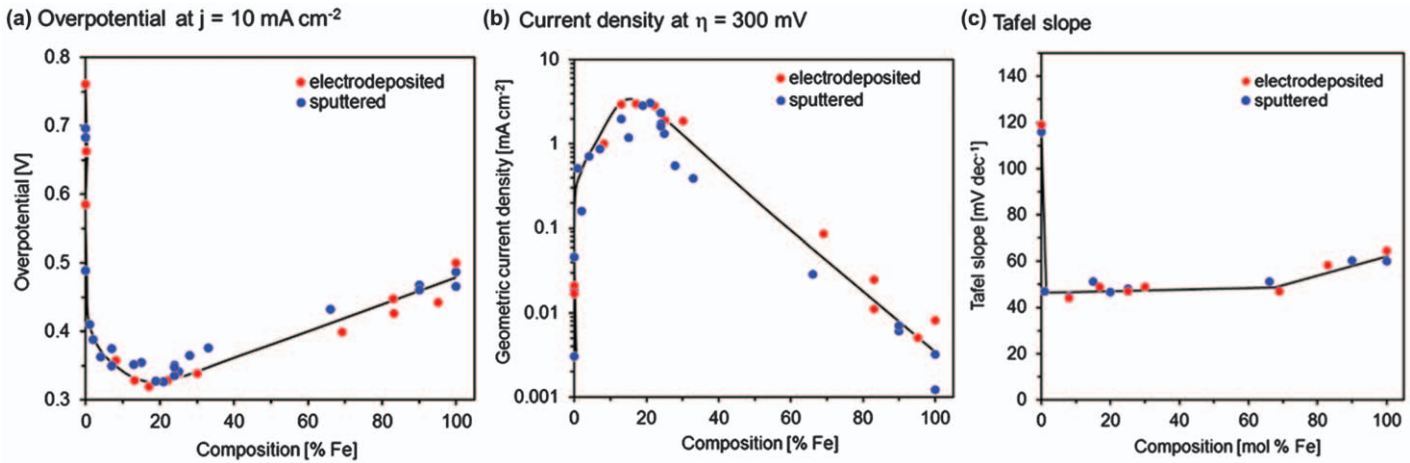

Figure 3.4 Activity plots for sputtered and electrodeposited $Ni_{1-x}Fe_xOOH$ films. Activity values were obtained after holding for 1 h at either constant (a) geometric current density (10 mA cm^{-2}), (b) overpotential (300 mV), or with (c) Tafel slopes obtained from 10 mV s^{-1} CV scans. Measurements were obtained in 0.1 M KOH with a RDE rotation rate of 1600 RPM. Curves are included to guide the eye.
Reprinted with permission from S. Klaus, M. W. Louie, L. Trotochaud and A. T. Bell, Role of Catalyst Preparation on the Electrocatalytic Activity of $Ni_{1-x}Fe_xOOH$ for the Oxygen Evolution Reaction, *J. Phys. Chem. C*, 2015, **119**, 18303–18316, Copyright 2015 American Chemical Society.[32]

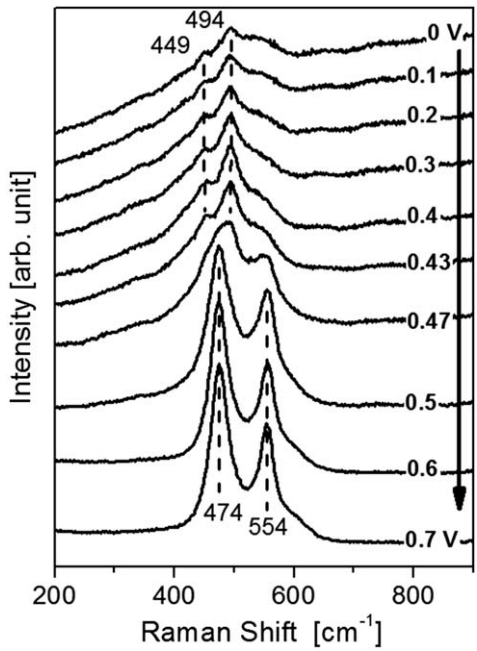

Figure 3.5 *In situ* Raman spectra for Ni films deposited on a roughened Au substrate as a function of potential *vs.* Hg/HgO (1 M KOH) in 0.1 M KOH, for which the equilibrium potential for the OER is 0.365 V.
Reprinted from M. W. Louie and A. T. Bell, An Investigation of Thin-Film Ni-Fe Oxide Catalysts for the Electrochemical Evolution of Oxygen, *J. Am. Chem. Soc.* 2013, **135**, 12329–12337, Copyright 2013 American Chemical Society.[15]

NiOOH (bands at 474 cm^{-1} and 554 cm^{-1}). This change is accompanied by a peak in the plot of current *vs.* voltage due to the process $Ni(OH)_2 + OH^- \rightarrow NiOOH + H_2O + e^-$, which results in the oxidation of Ni^{2+} to Ni^{3+}. It is noted that this process occurs below the potential for the onset of the OER. With progressive addition of Fe to the metal film, the Raman spectrum observed at 1.5 *vs.* RHE changes from that of NiOOH to that of FeOOH, as seen in Figure 3.6. This change is accompanied by a shift in the Ni^{2+} to Ni^{3+} oxidation peak to higher potentials for all samples containing Ni. The interpretation of this shift is discussed below.

Friebel *et al.* have characterized electrochemically deposited $FeNiO_x$ films by *operando* high energy resolution fluorescence detection X-ray adsorption spectroscopy (HERFD XAS).[34] The HERFD XAS spectrum of an Fe-only OER catalyst is shown in Figure 3.7a. The pre-edge region at ~7115 eV exhibits a small discrepancy in the characteristic double-peak structure for octahedrally coordinated Fe^{3+} as observed for γ-FeOOH.[35,36] This suggests that a small amount (10% ± 3%) of tetrahedrally coordinated Fe^{3+} may therefore exist in addition to a majority (90% ± 3%) of octahedrally coordinated Fe^{3+}.

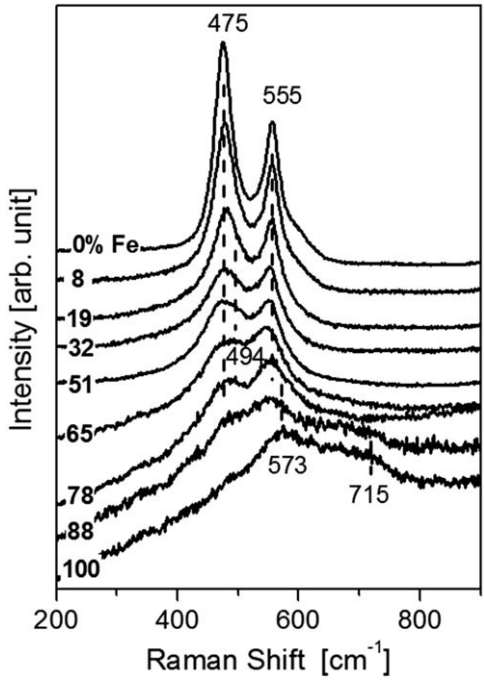

Figure 3.6 *In situ* Raman spectra collected in 0.1 M KOH at an OER overpotential of 0.235 V (or 0.6 V *vs.* Hg/HgO (1 M KOH)) for Ni–Fe films as a function of composition.
Reprinted from M. W. Louie and A. T. Bell, An Investigation of Thin-Film Ni-Fe Oxide Catalysts for the Electrochemical Evolution of Oxygen, *J. Am. Chem. Soc.* 2013, 135, 12329–12337, Copyright 2013 American Chemical Society.[15]

HERFD XAS measurements at potentials of 1.12 V, 1.52 V, 1.62 V, and 1.72 V (*vs.* RHE) show no evidence for potential-induced phase transformation in the pure FeOOH sample. By contrast, the Fe K-edge HERFD XAS for a sample containing 25% Fe and 75% Ni shows strong potential-induced changes (Figure 3.9b) that coincide with changes in the complementary Ni K-edge HERFD XAS spectra presented in Figure 3.7e. The latter are attributed to the spectral signatures of α-$Ni(OH)_2$ at low potentials and γ-NiOOH at high potentials.[37–42] Both α-$Ni(OH)_2$ and γ-NiOOH form layered structures of edge-sharing [NiO_6] octahedra separated by intercalated water molecules and hydrated ions (Figure 3.7d).[44] The Ni–O bond lengths[39–44] differ significantly between 2.05 Å in Ni(II)-containing α-$Ni(OH)_2$, and 1.88 Å in γ-NiOOH which is non-stoichiometric ($NiOOH_{1-x}$) and contains a mixture of Ni^{3+} and Ni^{4+} sites.[43] The significant shift of both the pre-edge peak and the main absorption edge in the Ni K-edge spectra (Figure 3.9e) shows nearly complete oxidation of Ni sites when the potential is increased from 1.12 to 1.52 V *vs.* RHE; the features of the oxidized component then approach saturation with further potential increase. A more detailed analysis confirmed that the

observed redox transition is between α-Ni(OH)$_2$ and γ-NiOOH and that the presence of β-Ni(OH)$_2$ or β-NiOOH can be ruled out.

Both the Fe and Ni K-edge spectra exhibit shifts of the structure-sensitive EXAFS dips and peaks to higher energy, indicating significant bond contraction. Using the 'bond length with a ruler' relationship $(E_{\text{peak}} - E_0)d^2 = \text{const.}$,[44,45] which is equivalent to an EXAFS analysis with a strongly reduced number of independent fitting parameters, the M–O bond length is estimated to contract by (7 ± 1)% for both Fe–O and Ni–O bonds. Complementary *operando* EXAFS measurements over a much larger energy range for an Fe/Ni (25:75) sample in the fully reduced and fully oxidized state are shown in Figure 3.8c. Analysis of these results confirms that the Fe–O and Ni–O bond lengths contract from 2.01 Å and 2.06 Å at 1.12 V to 1.90 Å and 1.89 Å at 1.92 V, respectively. A strong correlation was found not only between Fe–O and Ni–O bond lengths but also between nearest metal–metal distances, indicating that Fe substitutes for Ni in both α-Ni(OH)$_2$ and γ-NiOOH. Moreover, the identical appearance in both Fe and Ni K-edge EXAFS of a peak at approximately twice the nearest Ni–Ni and Fe–Ni distance, due predominantly to multiple-scattering in collinear Fe–Ni–Ni, Ni–Fe–Ni and Ni–Ni–Ni arrangements, clearly shows that Fe is not intercalated between the hexagonal [NiO_2] sheets but instead substitutes for Ni within the sheets.

The HERFD XAS also reveals information about the oxidation states of Fe and Ni in Fe-substituted α-Ni(OH)$_2$ and γ-NiOOH. Contracted bond distances are commonly associated with an increased oxidation state, and such oxidation state increase can be clearly seen in the Ni K-edge spectra where the pre-edge centroid and the photoionization threshold both shift to significantly higher energy. By contrast, an intriguing discrepancy can be seen in the Fe K-edge spectra. Comparison of the short Fe–O distance of (1.90 ± 0.01) Å at 1.62 V with bond lengths for different Fe oxides reported in the literature suggests that all Fe sites should have increased their oxidation state from +3 to +4. However, if such a significant oxidation state increase occurred at all Fe sites, a more noticeable shift to higher energies would have been expected for both the pre-edge centroid as well as the photoionization threshold. Further analysis shows that the features characteristic of Fe^{4+}, *e.g.*, a ligand-to-metal charge transfer (LMCT) shakedown feature near the main edge and a strong decrease of the white line intensity, are not observed for Fe-containing γ-NiOOH and is, therefore, concluded that the concentration of Fe^{4+} cation is small.

Ni–O and Fe–O bond length as a function of Fe content are presented in Figure 3.8a for two potentials, the resting state at 1.12 V as well as OER operating conditions at 1.62 V. Irrespective of the presence and concentration of Fe, the Ni–O bond lengths correspond to α-Ni(OH)$_2$ and γ-NiOOH at low and high potentials, respectively. Conversely, the average Fe–O bond length completely follows the Ni–O bond contraction only at low Fe content (10% and 25%). With increasing Fe content, the Fe–O distance at 1.62 V gradually increases towards that of pure γ-FeOOH. The results suggest that

two different Fe^{3+} species are present, *i.e.*, Fe^{3+} dopants in α-$Ni(OH)_2$/γ-NiOOH and Fe^{3+} sites within a separate γ-FeOOH phase. While a single Ni/Fe phase exists at low Fe content, FeOOH increasingly contributes to the

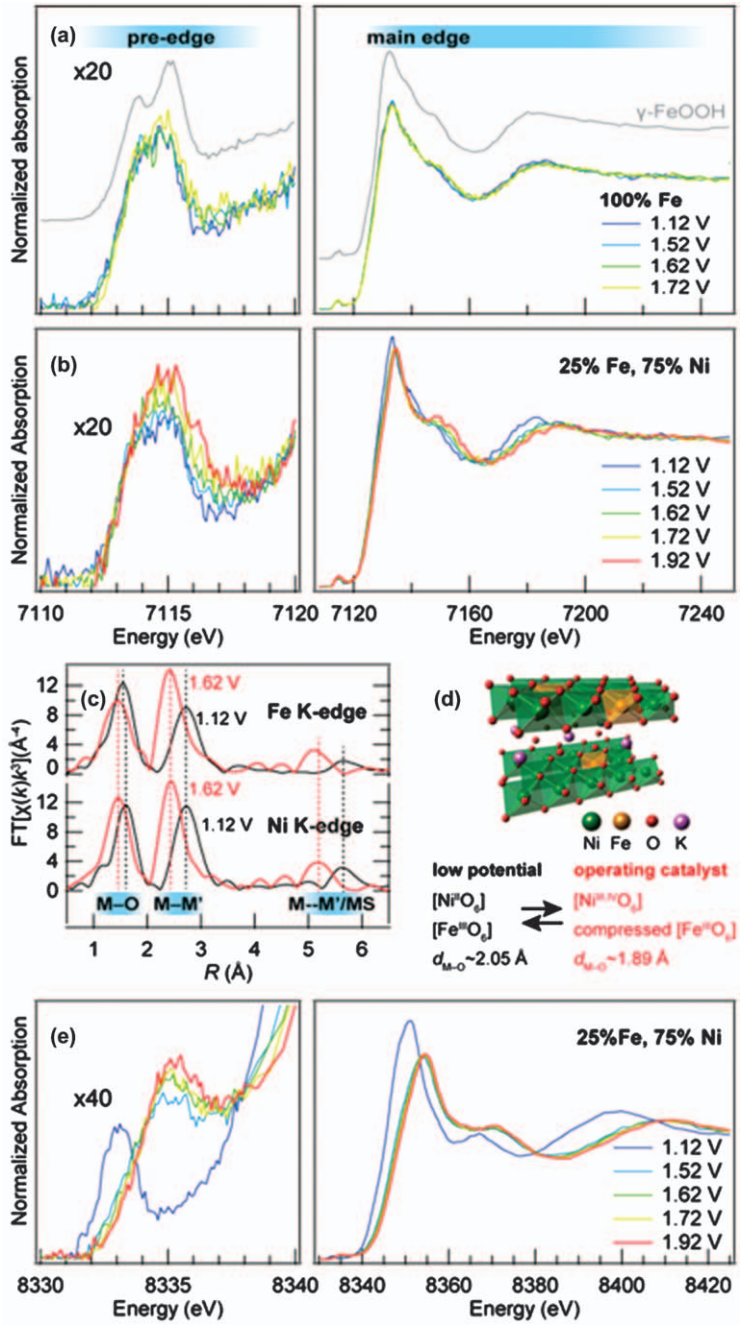

Fe K-edge spectra with increasing overall Fe content, due to limited solubility of Fe^{3+} in α-$Ni(OH)_2$. These results are consistent with the study of Fe uptake into $Ni(OH)_2$ from Fe-containing KOH solution presented above, which indicates a solubility limit near 25% Fe.[31] Since a Ni–O bond expansion even at 75% Fe content is not observed, it is estimated based on experimental uncertainty in the Ni–O bond distance, that Ni doping into γ-FeOOH, if any, does not exceed 3%. The model structures shown in Figure 3.8b capture the known oxidation states and local binding environment of metal sites. A comparison of theoretically predicted metal–oxygen bond lengths (Figure 3.8c) with the experimental values from our measurements (Figure 3.7a) and literature supports the hypothesis that only Fe-doped γ-NiOOH and pure FeOOH, but very little, if any, Ni-doped γ-FeOOH, exist under OER conditions.

The deductions concerning the charges of Fe and Ni cations and Fe–O and Ni–O bond distance determined by Friebel *et al.*[34] are supported by DFT + U calculations (see below for details). Löwdin charges of Ni, Fe, O, and H relative to the free atoms provide a measure of the apparent oxidation states of these elements. Figure 3.8d shows that the Löwdin charges for both Fe and Ni relative to the free atoms remain approximately constant for all model structures investigated. This finding agrees with the experimental observation that oxidation states of Fe and Ni under OER conditions are +3 and +3.6 (average), respectively, independent of the Ni/Fe ratio. The Löwdin charge for Fe is calculated to be significantly higher than for Ni despite the opposite order of formal oxidation states of both cations, which reflects the more ionic and less covalent nature of Fe–O than Ni–O bonds. Likewise, the linear increase in negative charge on the O atoms with increasing Fe content is attributable to the replacement of the more covalent Ni–O bonds with the more ionic Fe–O bonds.

Figure 3.7 Comparison of 100% Fe-containing sample with OER catalyst containing 25% Fe and 75% Ni using *operando* HERFD XAS. (a) Catalyst containing 100% Fe. The spectrum of γ-FeOOH is also shown for comparison. Plots of both pre-edge (enlarged) and the full spectra are shown. (b)-(e) Catalyst containing 25% Fe and 75% Ni. (b) Fe K-edge. While the potential increase does not influence the oxidation-state-sensitive energy of the main absorption threshold (7125 eV), significant Fe–O bond contraction with increasing potential is clearly indicated by the changes of the photoelectron scattering features (energy range above 7140 eV). (c) Complementary *operando* EXAFS measurement confirming the potential-induced bond contraction at both Fe and Ni sites. (d) Structure model of Fe-doped γ-NiOOH. (e) Ni K-edge XAS showing shifts in both oxidation-state-sensitive and structure-sensitive features due to oxidation of Ni^{2+} sites.
Reprinted from D. Friebel, M. W. Louie, M. Abjdich, K. E. Sewald, Y. Cai, A. M. Wise, M.-J. Cheng, D. Sokaras, T.-C. Weng, R. Alonso, R. C. Davis, J. R. Bargar, J. K. Nørskov, A. Nilsson and A. T. Bell, Identification of Highly active Fe Sites in (Ni,Fe)OOH for Electrocatalytic Splitting of Water, *J. Am. Chem. Soc.* 2015, **137**, 1305–1313, Copyright 2015 American Chemical Society.[34]

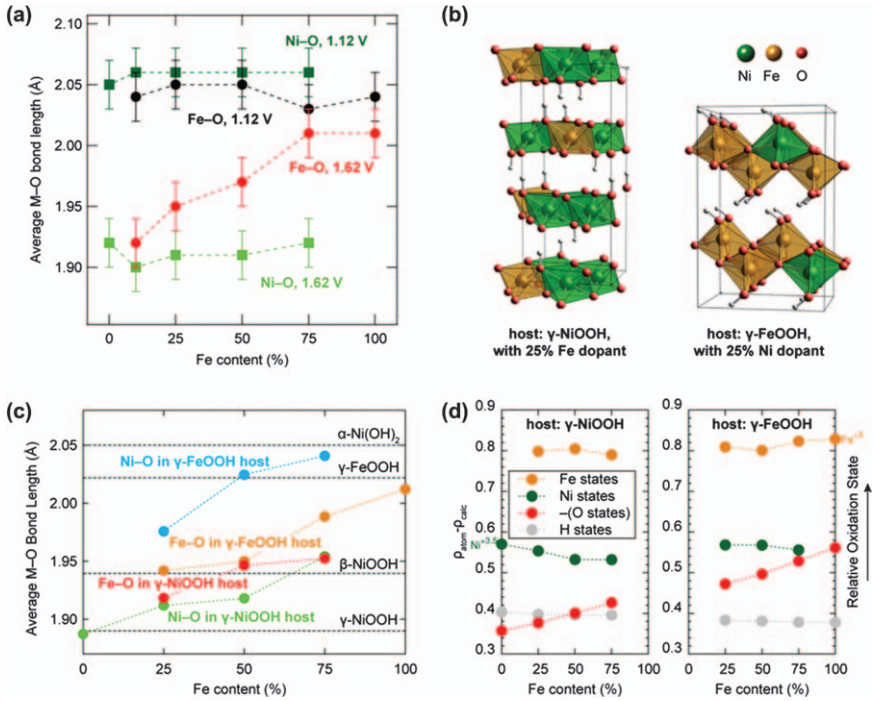

Figure 3.8 Identification of the most likely structural motif for mixed Ni,Fe catalysts by comparison of experimentally obtained metal–oxygen bond lengths with optimized theoretical model structures. (a) Bond lengths extracted from HERFD XAS measurements at 1.12 V and 1.62 V, plotted as a function of Fe content. (b) Examples of unit cells for Fe-substituted γ-NiOOH and Ni-substituted γ-FeOOH model structures. (c) Theoretically predicted bond lengths, corrected by a factor of 0.97 for comparison with experimental data. The dashed lines represent experimental bond lengths from literature. (d) Löwdin charges in Fe-substituted γ-NiOOH and Ni-substituted γ-FeOOH model structures, plotted as a function of Fe content. All dashed lines are guides to the eye.
Reprinted from D. Friebel, M. W. Louie, M. Abjdich, K. E. Sewald, Y. Cai, A. M. Wise, M.-J. Cheng, D. Sokaras, T.-C. Weng, R. Alonso, R. C. Davis, J. R. Bargar, J. K. Nørskov, A. Nilsson and A. T. Bell, Identification of Highly active Fe Sites in (Ni,Fe)OOH for Electrocatalytic Splitting of Water, *J. Am. Chem. Soc.* 2015, **137**, 1305–1313, Copyright 2015 American Chemical Society.[34]

The DFT + U calculations reported by Friebel *et al.*[34] also confirm that an Fe–O bond distance similar to that for Ni–O should be observed when Fe^{3+} cations substituted for Ni^{3+} cations in γ-$Ni_{1-x}Fe_xOOH$. The absence of any experimental evidence for Ni–O bond expansion in materials prepared with Fe contents above 50% suggests that for Fe contents in excess of ~25%, a γ-FeOOH phase is nucleated that does not contain a large amount of Ni in it. The differences in solubility limits for Fe in $Ni(OH)_2$/NiOOH and Ni in FeOOH are attributed to differences in the capability of the host structures to

compensate the charge difference between Ni^{2+} and Fe^{3+} which are present at low potential and, presumably, during catalyst electrodeposition. The α-$Ni(OH)_2$ structure contains intercalated H_2O between the hexagonal [NiO_2] sheets, and can accommodate electrolyte anions. In the resulting charge-neutral $Ni(II)_{1-x}Fe(III)_x(OH)_{2+x}(H_2O)_y$ layered double hydroxide structure,[46] Fe uptake is enabled by closely matching Fe^{3+}–O and Ni^{2+}–O distances but limited by steric hindrance and repulsion between partially hydrated anions. Conversely, there is no obvious pathway for the γ-FeOOH structure to allow intercalation of cations (*e.g.*, K^+) or protonation of O or OH ligands without a significant distortion of linkages between [MO_6] octahedra. Correspondingly, the absence of intercalation in β-$Ni(OH)_2$ could explain why the presence of Fe^{3+} appears to prevent the transformation ('aging') of α-$Ni(OH)_2$ into β-$Ni(OH)_2$.[30]

It is important to compare and contrast the findings of Friebel *et al.*[34] with those recently reported by Strasser and coworkers,[47] who estimated the oxidation state of Ni and Fe from quantitative deconvolution of the charge injected into $Ni_{1-x}Fe_xOOH$ during cyclic voltammetry (CV) complemented by data from differential electrochemical mass spectrometry (DEMS) and from analysis of *ex situ* X-ray absorption measurements (XAS). These authors found that in the absence of intentional Fe addition, the CV data lead to the conclusion that all of the Ni^{2+} undergoes oxidation to Ni^{3+}, whereas the DEMS data suggest that up to 25% of the Ni reaches the Ni^{4+} oxidation state. The addition of Fe stabilized low-valent Ni and suppressed its oxidation to higher oxidation states. These findings are qualitatively consistent with the findings of Friebel *et al.* determined from *operando* XAS.[34]

The XAS data reported by Strasser and coworkers[47] were obtained by freeze-quenching catalysts after conditioning them at 1.63 V *vs.* RHE. The Ni K-edge position observed in the XANES spectrum of freeze quenched NiO_x was consistent with an oxidation state of +3.7 but the oxidation state was reported to decrease to +2 with the addition of more than 4% Fe. It is notable that the Ni–O distance determined EXAFS data for freeze-quenched NiO_x was 1.88 Å but increased to 2.05 Å with the addition of more than 4% Fe. The Fe K-edge position observed in the XANES spectrum of freeze-quenched FeO_x was consistent with an Fe oxidation state of +3.4, and little change in oxidation state was observed when Fe was present together with Ni. Likewise, the Fe–O distance determined from analysis of the EXAFS data gave a value of 2.0 Å independent of whether Fe was present alone or together with Ni.

The oxidation states of Ni and Fe and the corresponding Fe–O and Ni–O bond distances reported by Strasser and coworkers[47] for NiOOH and FeOOH agree reasonably well with those reported by Friebel *et al.*;[34] however, significant differences occur for all samples of $Ni_{1-x}Fe_xOOH$. Whereas the *operando* EXAFS data of Friebel *et al.*[34] show that the Ni–O bond distance retains its value in NiOOH upon the addition of Fe, the freeze-quenched samples examined *ex situ* by Strasser and coworkers[47] show Ni–O bond distances that are more characteristic of $Ni(OH)_2$, a conclusion that would be

fully consistent with their observation that Ni is in the 2+ state for these samples. Likewise, whereas Friebel *et al.* find that the Fe–O bond distance in $Ni_{1-x}Fe_xOOH$ undergoes a contraction from 2.01 Å to 1.90 Å for low values of x and then monotonically increases as x increases (see Figure 3.8), Strasser and coworkers[47] find that the Fe–O bond distance remains at about 2.00 Å independent of the value of x. What these findings suggest is that freeze quenching of $Ni_{1-x}Fe_xOOH$ samples after their use for electrochemistry cannot give reliable information about the environments of Ni and Fe cations.

3.5 Identity of the Active Site in $FeNiO_x$

Not addressed to this point is why the substitution of Fe^{3+} into the lattice of γ-NiOOH increases the OER activity. Two options exist—one is that the substituted Fe^{3+} sites become more active when hosted in the lattice of γ-NiOOH due to a change in their electronic environment and the other is that the activity of Ni^{3+} sites becomes more active as a consequence of their electronic properties being altered by the substitution of Fe^{3+} cations into the γ-NiOOH lattice. Another question to ask is whether the small amount of Ni^{3+} that can substitute into γ-FeOOH has an effect on the OER activity of this phase, and if so, how so? As discussed next, both sets of questions can be addressed by DFT + U calculations of the overpotential for the OER.

Friebel *et al.*[34] have reported DFT + U calculations aimed at developing a deeper understanding of the effects of Fe substitution into γ-NiOOH and Ni substitution into γ-FeOOH. Their approach builds on procedures developed by Nørskov and coworkers, which have been demonstrated to give a solid basis for interpreting the relationship between catalyst composition and OER overpotential.[48–50] In acidic conditions, the OER is taken to occur *via* four elementary steps:

$$H_2O + * \rightarrow OH^* + e^- + H^+ \quad (3.1)$$

$$OH^* \rightarrow O^* + e^- + H^+ \quad (3.2)$$

$$O^* + H_2O \rightarrow OOH^* + e^- + H^+ \quad (3.3)$$

$$OOH^* \rightarrow O_2 + e^- + H^+ \quad (3.4)$$

where * indicates an oxygen vacancy site at the surface. It should be noted that this sequence of steps is based on chemical intuition developed from studies of the oxygen reduction reaction on metals, rather than direct observation of the postulated intermediates involved in the OER occurring over NiFeOOH. While several attempts to identify intermediates involved in the OER by *operando* Raman spectroscopy have been reported, these studies have only observed weak evidence for peroxo/superoxo species. For this reason, theoretical analyses have utilized the scheme shown above.

The chemical potentials of protons and electrons at any given pH and applied potential E were described by the computational hydrogen electrode.[48] As a consequence, the theoretical overpotential η_{OER} obtained from Gibbs free energy differences ΔG_i $(i = 1...4)$ at each step is independent of pH and is therefore applicable to alkaline conditions.

$$\eta_{OER} = \max[\Delta G_1, \Delta G_2, \Delta G_3, \Delta G_4]/e - 1.23\ [\mathrm{V}] \tag{3.5}$$

Figure 3.9 compares predicted overpotentials for the OER occurring at Ni and Fe surface sites in pure and doped γ-NiOOH and γ-FeOOH. The results shown in Figure 3.9 can be rationalized in terms of the overall affinity of surface sites for adsorbed intermediates and the relative stability of O* with respect to OH* and OOH*. Generally, much weaker adsorption is found for the on-top position of a single 5-fold coordinated metal atom than for the bridge site between two 5-fold coordinated metal atoms, and Fe sites have significantly higher OH affinity than Ni sites. While the difference between adsorption energies of OH* and OOH* is nearly constant, $\Delta E_{OOH} = 0.8\Delta E_{OH} + 3.3$ eV, the O* binding energy increases as function of ΔE_{OH}. Under the optimum condition $\Delta E_O - \Delta E_{OH} = 0.5(\Delta E_{OOH} - \Delta E_{OH})$,[50] η_{OER} reaches a minimum value of 0.4 V. In the absence of cation substitution, all OER intermediates adsorb too strongly on pure γ-FeOOH and too weakly on pure γ-NiOOH. The calculated overpotentials for Fe-free γ-NiOOH are larger than that for pure γ-FeOOH.

Compared to pure γ-FeOOH, Fe sites surrounded by Ni next-nearest neighbors in either γ-NiOOH or γ-FeOOH host structures exhibit decreased affinity for OER intermediates, resulting in a shift in their binding energies towards optimal values. The origin of these trends can be rationalized based on the results in Figure 3.8d, which show that $Ni^{3+/4+}$ cations, due to their higher electron affinity compared to Fe^{3+}, withdraw electron density from oxygen sites. During OER, the formation of HO* and O* requires an oxidation state increase at the active Fe site, which becomes evident, for example, in the notably short bond distance of 1.62 Å between O* and a highly charged Fe site in Fe-doped γ-NiOOH $(01\bar{1}\ 2)$ (Figure 3.9a). The oxidation of the Fe surface site will be less favorable energetically in γ-NiOOH than in γ-FeOOH, because neighboring Ni sites induce lower negative charge density on adsorbed O and OH. We propose that this effect is mostly determined by the local arrangement of neighboring Fe and Ni sites. Computational results for structurally similar Ni-doped hematite indicate the same mechanism for the catalytic enhancement, further supporting our hypothesis.[51]

Further calculations comparing the overpotentials for the OER occurring over Ni or Fe sites confirm that Fe rather than Ni constitutes the active site for the OER at mixed Fe–Ni oxyhydroxides. Subsurface Fe sites in γ-NiOOH (Figure 3.9b) increase the OER overpotential at Ni surface sites because the already too weak oxygen affinity of Ni further decreases. This finding is consistent with the experimentally observed shift of the α-$Ni(OH)_2$/γ-NiOOH redox potential to higher values with increasing Fe content.[15]

The results presented in Figure 3.9 are consistent with those of Li and Selloni,[52] who have reported DFT + U calculations of the OER overpotentials for β- and γ-NiOOH and for Fe substituted into the surface of both NiOOH phases. While the catalyst structure used by these authors differ

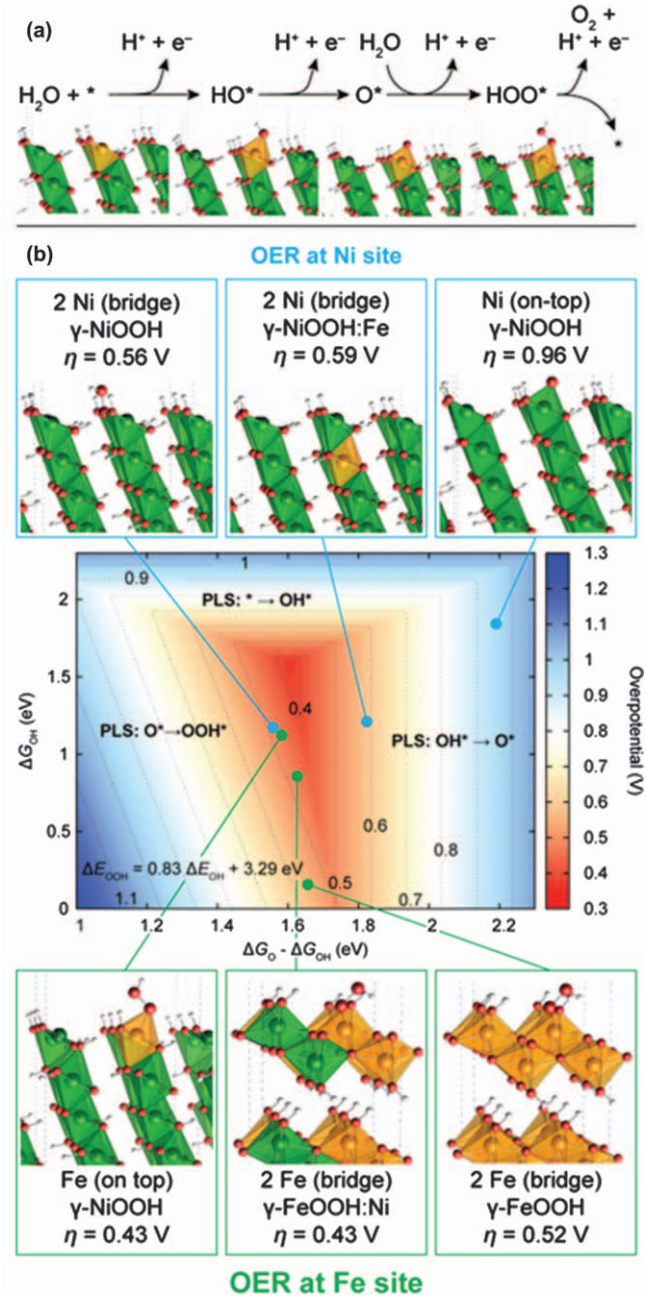

substantially from that used by Friebel *et al.*, both studies agree that the OER overpotential for Fe-doped γ-NiOOH is lower than that for pure γ-NiOOH. Thus, Li and Selloni[54] find that $\eta = 0.48$ V for Fe-doped γ-NiOOH and $\eta = 0.52$ V for pure γ-NiOOH, whereas Friebel *et al.*[34] find that $\eta = 0.43$ V for Fe-doped γ-NiOOH and $\eta = 0.56$ V for pure γ-NiOOH. Li and Selloni[54] also predict that an even lower overpotential for the OER could be achieved on Fe-doped β-NiOOH ($\eta = 0.26$ V) and that the overpotential for pure β-NiOOH should be lower than that for γ-NiOOH ($\eta = 0.46$ V for β-NiOOH *versus* $\eta = 0.52$ V for γ-NiOOH). While these are interesting findings, it should be noted that Friebel *et al.*[34] did not find any experimental evidence for the β phase of NiOOH, and work by Trotochaud *et al.* has shown that the presence of Fe in the active phase of Ni–Fe oxides inhibits the formation of this phase.[30]

Theoretical analysis of the effects of Fe^{3+} substitution for Ni^{3+} in NiOOH has also been reported by Koper and coworkers.[10] In these studies NiOOH was represented by NiO terminated on the (001) surface by *O and *OH. The extent of Fe^{3+} substitution was chosen to be 50%. Based on this model, the potential-limiting value of η_{OER} was found to be 0.37 V for Fe^{3+} cations and 0.57 V for Ni^{3+} cations in qualitative agreement with the findings of Li and Selloni[54] and of Friebel *et al.*[34]

The conclusions of the theoretical analyses reported above have recently been confirmed by experiments reported by Ahn and Bard,[53] using scanning electrochemical microscopy to determine the kinetics of the OER on Ni and Fe cations in NiOOH, FeOOH, and $Ni_{1-x}Fe_xOOH$ ($0 < x < 0.27$). The active centers were assumed to be in the 4+ state. Table 3.1 presents the rate coefficients for the dynamics of oxygen evolution on 'fast' and 'slow' sites.

Figure 3.9 Theoretical OER overpotentials at Ni and Fe surface sites in pure and doped γ-NiOOH and γ-FeOOH model structures. (a) Proposed OER pathway with intermediates HO*, O* and HOO*, illustrated using the example of the on-top site at a substituted Fe surface atom in γ-NiOOH ($01\bar{1}2$). The binding energies of these species are used to estimate the OER overpotential. (b) OER activity volcano plot showing the overpotential as a function of Gibbs free energies of the reaction intermediates. Computed overpotentials are shown for the OER at Ni–Ni bridge and Fe on-top sites located in pure γ-NiOOH ($01\bar{1}2$) and in γ-NiOOH ($01\bar{1}2$) with Fe surface and subsurface doping, at a Ni on-top site in pure γ-NiOOH ($01\bar{1}2$), and at Fe–Fe bridge sites in pure and Ni-doped γ-FeOOH (010) (25% Ni in bulk unit cells). All corresponding model structures are shown with the intermediate whose formation is the potential limiting step (PLS) (HOO* in all cases except for the on-top Ni site in γ-NiOOH ($01\bar{1}2$) and γ-NiOOH ($01\bar{1}2$) with subsurface Fe, where formation of O* determines the overpotential).
Reprinted from D. Friebel, M. W. Louie, M. Abjdich, K. E. Sewald, Y. Cai, A. M. Wise, M.-J. Cheng, D. Sokaras, T.-C. Weng, R. Alonso, R. C. Davis, J. R. Bargar, J. K. Nørskov, A. Nilsson and A. T. Bell, Identification of Highly active Fe Sites in (Ni,Fe)OOH for Electrocatalytic Splitting of Water, *J. Am. Chem. Soc*. 2015, **137**, 1305–1313, Copyright 2015 American Chemical Society.[34]

Table 3.1 Pseudo-first-order OER rate constants.[53]

Catalyst	Fe Content (%)	'Fast' site rate constant k' (s^{-1})	'Slow' site rate constant k' (s^{-1})	'Fast' site fraction (%)
NiOOH	<0.8	0.04 ± 0.03		
$Ni_{0.91}Fe_{0.09}OOH$	8.97	0.41 ± 0.03	0.01 ± 0.02	6.4
$Ni_{0.82}Fe_{0.18}OOH$	18.97	1.70 ± 0.07	0.04 ± 0.02	17.6
$Ni_{0.73}Fe_{0.27}OOH$	27.31	0.34 ± 0.17		
FeOOH	>98.3	0.18 ± 0.05	0.02 ± 0.02	8.6

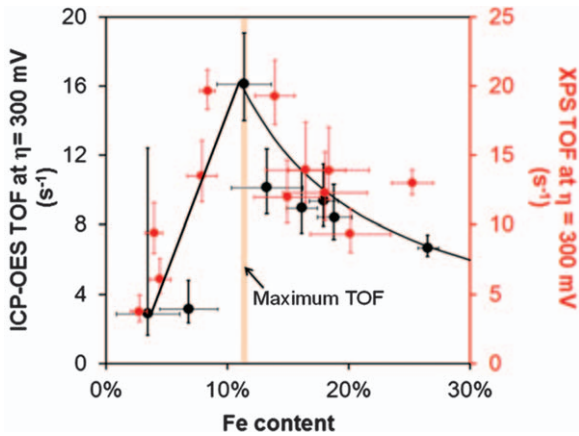

Figure 3.10 Turnover frequency (calculated on a per-Fe site basis) from total Fe content (ICP-OES: black, XPS: red) for $Ni(OH)_2$ films deposited on polished Au-RDEs as a function of percent Fe. The solid line represents the anticipated TOF assuming Fe content exceeding 11% is not OER-active. Error bars are determined from the inherent uncertainty in the Fe content as determined by ICP-OES and XPS for each sample.
Reprinted with permission from S. Klaus, Y. Cai, M. W. Louie, L. Trotochaud and A. T. Bell, Effects of Fe Electrolyte Impurities on $Ni(OH)_2$/NiOOH Structure and Oxygen Evolution Activity, *J. Phys. Chem. C* 2015, **119**, 7243–7254, Copyright 2015 American Chemical Society.[31]

The rate constant for oxygen evolution on 'fast' sites in NiOOH is comparable to that measured for 'slow' sites in $Ni_{1-x}Fe_xOOH$ and a factor of 4.5 lower than that for 'fast' sites in FeOOH. With increasing substitution of Fe for Ni in $Ni_{1-x}Fe_xOOH$, the magnitude of the rate coefficient for 'fast' sites increases up to $x = 0.18$ and then decreases for $x = 0.27$, leading to the conclusion that the 'fast' sites are attributable to Fe cations, whereas the 'slow' sites are attributable to Ni cations.

The increase in the apparent rate coefficient for oxygen evolution on 'fast' sites with increasing Fe content reported by Ahn and Bard[53] (see Table 3.1) is fully consistent with the turnover frequency for OER reported by Klaus *et al.*[31] and shown in Figure 3.10. Most notably, both studies demonstrate

that with increasing addition of Fe to NiOOH, the apparent rate coefficient for the OER increases up to a maximum value and then declines. As noted earlier the Fe content at which the maximum occurs depends on the manner of sample preparation. These findings suggest that up to the solubility limit of Fe^{3+} cations in NiOOH, the activity of each Fe cation increases due to subtle changes in its environment, a subject not yet fully understood and requiring further investigation.

It is notable that while Ahn and Bard[53] suggest that the oxidation state of the 'fast' Fe sites in $Ni_{1-x}Fe_xOOH$ is +4, based on the observation of this state in XAS studies, no direct evidence for the involvement of Fe^{4+} in OER was presented. In fact, recent work by Stahl *et al.*[54] suggests that, to the contrary, Fe^{3+} cations are the active centers. This conclusion was reached on the basis of *operando* Mössbauer spectroscopy. While direct evidence for Fe^{4+} cations in $Ni_{1-x}Fe_xOOH$ was observed, the persistence of these cations upon lowering the potential during *operando* OER studies, suggests they are not directly responsible for oxygen evolution. This conclusion supports the theoretical findings that indicate the OER occurs preferentially on Fe^{3+} cations.

3.6 Factors Affecting the OER Activity of NiFeOOH

A very large number of papers that have appeared in the recent literature describing different methods for preparing NiFeOOH OER catalysts.[55–78] These include electrodeposition and sputter deposition of thin metal films that upon immersion in alkaline electrolyte convert to the hydroxide phase and to the oxy-hydroxide upon application of a sufficiently high anodic potential, preparation of NiFeOOH nanoparticles by solvothermal or hydrothermal co-precipitation of mixed metal precursors, and pulsed-laser ablation of metals in liquids (PLAL). Comparison of the OER performance of NiFeOOH catalysts prepared by different methods is challenging, since many factors affect their activity.

To understand what factors influence the performance of NiFeOOH catalysts, we begin by noting that in the absence of mass transfer limitation the dependence of the current density based on the geometric area of the anode is described by the Butler–Volmer equation, which for large values of η_{OER}, is given by:[79]

$$j = j_0 \exp\left(\frac{\alpha z F}{RT}\eta_{OER}\right) \tag{3.6}$$

where j_0 is the exchange current density, R is the gas constant, T is the temperature, α is the transfer coefficient, z is the number of electrons transferred in the rate-limiting step, and F is Faraday's constant. The value of j_0 is proportional to the number of electrochemically active centers per unit weight of catalyst placed on the anode, which is, in turn, proportional to the weight of catalyst deposited per unit anode area. If all of the active centers are assumed to be located at the external surface of the catalyst, then the

number of electrochemically active centers per unit weight of catalyst should be related to the BET surface area (surface area per unit weight of catalyst). However, the underlying assumption for this relation has been questioned, since active centers can be located between the layers of the NiFe double hydroxide, as well as on the internal surface.[7,22] Further complicating matters is the recognition that the BET area of nanoparticles is rarely reported in experimental studies of OER catalysts and can be difficult to measure if the quantity of catalyst prepared is small. Similar complications arise with the alternative proposal that the surface area of the catalyst relative to surface of the anode can be described by the electrochemically determined roughness factor, since this quantity is also difficult to measure accurately. Yet further complications arise from the fact that the value of j_0 also depends on the intrinsic activity of the catalyst, which is dependent on the content of Fe and its distribution between $Ni_{1-x}Fe_xOOH$ and FeOOH.[34] Another factor not taken into account is the dependence of j_0 on the concentration of base. For KOH, j_0 is proportional to the concentration of OH^- anions for $pH > 11$.[15] Recent evidence also indicates that the composition of the electrode on which either thin films or nanoparticles of NiFeOOH are deposited can have a significant effect on j_0.[7,16] The preceding discussion shows that many factors in addition to the intrinsic activity of the catalyst affect the value of j_0 and consequently the observation of a lower value of η_{OER} for a given current density does not necessarily mean that the intrinsic activity of the material is superior to another one with a higher value of η_{OER}.

The dependence of η_{OER} on j is characterized by the Tafel slope, β, which is defined as the gradient in the ohmic-drop-corrected value of η_{OER} with respect to the logarithm of the current density (eqn (3.7)).[79]

$$\frac{d\eta_{OER}}{d\ \log(j)} = \frac{2.3\ RT}{\alpha z F} = \beta \tag{3.7}$$

Eqn (3.7) shows that the lower the Tafel slope, the more rapid the rise in current density. While the Tafel slope of OER catalysts is often reported, the range of current densities for which it is valid is usually not given.

It should be noted that inherent in the use of the Butler–Volmer equation and the determination of β from the Tafel slope is the assumption that a single charge transfer step dictates the overall kinetics of the OER and that all other steps are equilibrated. As discussed below, this assumption greatly simplifies the expression for the dependence of j on η_{OER}, but is overly constraining. Nevertheless, eqn (3.6) and (3.7) continue to be used because experimental data can often be described by these equations over a reasonable range of measured overpotentials.

Until very recently, attempts to interpret the magnitude of measured Tafel slopes have focused on postulating a reaction mechanism, assuming a rate-limiting step, and then determining the Tafel slope from a microkinetic model.[80,81] Agreement between the Tafel slope derived by this means and that measured experimentally was then used to rationalize the nature of the

rate-limiting step. This approach has very limited value, since dependence of the rate coefficients for elementary processes involving charge transfer on the potential applied to the cathode are assumed but are not based on a first-principles analysis of the relevant physics. Very recent work by Goddard and coworkers has illustrated a sounder, more physically correct approach.[82] In this study, rate coefficients for the elementary reactions involved in the OER on IrO_2 under acidic conditions are predicted from first principles using quantum mechanics. The authors find that for the reaction conditions used in experimental investigations of the OER, the IrO_2 (110) surface is fully O terminated and the rate-limiting step for O_2 formation involves the attack of aqueous water on a surface O atom leading to the dissociation of water and the formation of OOH*. Two possible pathways for this reaction are found, one for low (<1.5 V) and another for high (>1.5 V) applied potentials. A microkinetic model is then used to develop the relationship between current density and η_{OER}. The Tafel plot of η_{OER} *versus* $\ln(j)$ determined by this means exhibits two linear regimes. Above $\eta_{OER} = 0.35$ V, the Tafel slope is 73 meV per dec and below $\eta_{OER} = 0.3$ V, the Tafel slope is 22 meV per dec, in good accord with experimental observation. This work demonstrates that in order to understand the dependence of the current density on the OER overpotential, it is essential to carry out a detailed analysis of the free energies of activation for the OER processes and their dependence on the applied voltage.

The preceding discussion demonstrates why it is so difficult to compare the intrinsic activity of NiFeOOH catalysts prepared by different techniques. For this reason, most authors simply report the values of η_{OER} and β for a specified current density (usually 10 mA cm^{-2}) measured in a KOH solution of specified molarity (usually 0.1 M). From such measurements, it is possible to say that the catalyst with the lowest values of η_{OER} and β is the most active one.

3.7 Effects of Additives Other Than Fe on the OER Activity of $NiMO_x$

Numerous authors have investigated the extent to which elements other than Fe could be added to NiOOH in order to enhance its OER activity.[6,8,10,83–87] It should be noted, though, that all of these studies were conducted using KOH as the electrolyte and many were undertaken prior to the recognition that solutions of this base contain impurity Fe^{3+} cations that can incorporate into NiOOH and thereby increase its OER activity. Thus, the degree to which earlier studies are corrupted by Fe is not clear and for this reason, reliable conclusions about the effects of additive metals should be drawn from studies reported after 2014.

Koper and coworkers have examined the incorporation of Co, Fe, Mn, Cr, Cu, and Zn into NiOOH.[10] Based on DFT analysis of the potential limiting value of η_{OER}, they concluded that the incorporation of Mn should be

equivalent to the incorporation of Fe, and that of the remaining elements, only Cr enhances the OER of NiOOH. The order of decreasing activity was predicted to be NiFeOOH > NiMnOOH > NiCrOOH, and this sequence was confirmed by experimental observation. It is also notable that DFT analysis revealed that Fe and Mn are the active sites in NiFeOOH and NiMnOOH but Ni is the active site in NiCrOOH.

In a recent study, Boettcher and coworkers have investigated the effects of adding ~10% and 30% Fe, Mn, La, Ti, or Ce on the OER activity of NiOOH.[88] Catalyst films were prepared by spin-casting from solutions of 0.1 M $Ni(NO_3)_2 \cdot 6H_2O$ and the nitrate salt of the additive metal dissolved in a 1 : 1 mixture of ethanol and water onto Au/Ti or Pt/Ti coated quartz substrates. The coated substrates were then transferred to a hot plate maintained at 150 °C and annealed for 10 min. Following preparation, samples were characterized electrochemically by cycling in Fe-free 1 M KOH at 20 mV s^{-1}. Figure 3.11 illustrates the TOF_{tm} based on total metal content of each sample, taken after 5 and 50 voltammogram cycles. It is observed that after 5 cycles, the activities of the $Ni_{0.85}Ce_{0.15}O_xH_y$ and $Ni_{0.65}Ce_{0.35}O_xH_y$ films are about 8 and 4 times higher that of NiO_xH_y, respectively. However, after 50 cycles, the activity of $Ni_{0.85}Ce_{0.15}O_xH_y$ is only 2-fold higher than that of NiO_xH_y and the activity of $Ni_{0.65}Ce_{0.35}O_xH_y$ is equivalent to that of NiO_xH_y.

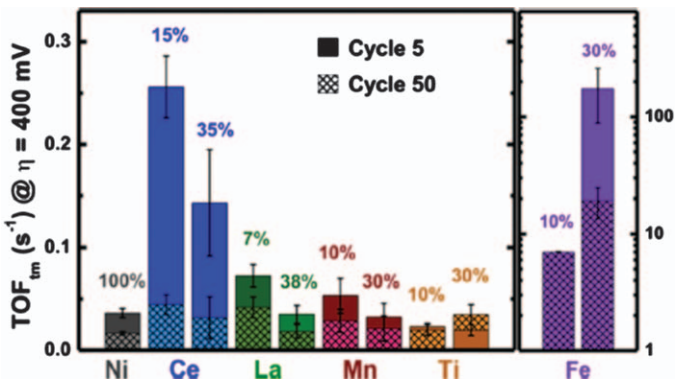

Figure 3.11 OER turnover frequency of spin-cast $Ni_{1-z}M_zO_xH_y$ films at 400 mV overpotential at cycle 5 (solid) and cycle 50 (pattern) in Fe-free 1 M KOH from voltammetry data collected at 20 mV s^{-1}. Values reported are the average, and error bars are the standard deviation of three samples. In the case of $Ni_{0.9}Fe_{0.1}O_xH_y$, there is no activity decrease over 50 cycles, and the error bars are small and not visible on this scale. TOFs are calculated assuming all metal cations are active (and thus are lower limits), and the OER current is taken as the average of the forward and reverse scans. Note the different scale on the *y*-axis for $Ni_{1-z}M_zO_xH_y$ films.
Reprinted from L. J. Enman, M. L. Burke, A. S. Batchellor and S. W. Boettcher, Effects of Intentionally Incorporated Metal Cations on the Oxygen Evolution Electrocatalytic Activity of Nickel (Oxy)hydroxide in Alkaline Media, *ACS Catal.* 2015, **6**, 2416–2423, Copyright 2015 American Chemical Society.[88]

The authors suggest that slow dissolution of Ce from the Ni(Ce)O_xH_y films may be the cause for the decrease in activity with cycling or alternatively that cerium oxide phase segregation occurs during electrochemical cycling. On the other hand, catalysts containing Ti, Mn, or La were found to have lower OER activities than NiO_xH_y. In contrast, Ni(Fe)O_xH_y films maintained their activity over the 50 cycles and were more than two orders of magnitude more active than NiO_xH_y. It was also noted that there was no significant correlation between the potential at which Ni^{2+}/Ni^{3+} redox occurred, suggesting that Ni is not the primary site for the OER. This finding is consistent with Fe being the active site in Ni(Fe)O_xH_y.

3.8 Effects of Additive on the OER Activity of $NiFeO_x$

A number of recent studies have examined the possibility of improving the OER activity of $NiFeO_x$ catalysts through the addition of a third metallic element. These efforts have utilized high-throughput methods to produce very large arrays of catalyst compositions, as described in greater detail in Chapter 9 by Gregoire, as well as targeted syntheses of specific catalyst compositions. Both approaches will be reviewed.

Stahl and coworkers have used a fluorescence-based combinatorial array to detect oxygen evolution from arrays of metal oxide catalysts.[89,90] Twenty-one ternary metal oxides were screened, each ternary oxide comprising twenty-one incremental compositions. Comparison of different ternary oxides containing Ni and Fe revealed that catalysts with compositions $Ni_{0.2}Fe_{0.4}Al_{0.4}O_x$, $Ni_{0.2}Fe_{0.4}Cr_{0.4}O_x$, and $Ni_{0.2}Fe_{0.2}Ga_{60}O_x$ were significantly more active at a fixed overpotential than one with the composition $Ni_{60}Fe_{0.4}O_x$. The Tafel slopes for $Ni_{0.2}Fe_{0.4}Al_{0.4}O_x$, $Ni_{0.2}Fe_{0.4}Cr_{0.4}O_x$, and $Ni_{0.2}Fe_{0.2}Ga_{60}O_x$ were in the range of 30–38 mV per dec.

As detailed in Chapter 9 in this book, an array of 5456 quaternary metal oxides containing Ni, Fe, Co, and Ce were explored by Haber *et al.*[91,92] at 3.3% atomic percent intervals. These samples were prepared by ink-jet printing on an FTO plate and each composition was then characterized by using a scanning drop three-electrode system. Of this set, 665 compositions were found to have superior activities than other combinations. Two samples were found to be exceptionally active and exhibited the same OER overpotential at a current density of 10 mA cm^{-2} – $Ni_{0.5}Fe_{0.3}Co_{0.17}Ce_{0.03}O_x$ and $Ni_{0.3}Fe_{0.07}Co_{0.2}Ce_{0.43}O_x$, which are referred to as low-Ce and high-Ce catalysts, respectively. The Tafel slopes for the low-Ce and high-Ce catalysts are approximately 40 mV per dec and 70 mV per dec, respectively. This illustration demonstrates that neither η_{OER} nor the Tafel slope can be used individually to identify catalyst activity, since the high-Ce catalyst is more active at low OER overpotentials but the low-Ce catalyst is more active at high OER overpotentials. Given the unexpected high activity of the high-Ce catalyst at low OER overpotentials, further investigation of this material was undertaken.[93] *Ex situ* synchrotron X-ray absorption spectroscopy (XAS) and low-dose, high-resolution transmission electron microscopy (TEM)

revealed that the catalyst is biphasic—consisting of distinct nano-domains of crystalline CeO_2 and particles having a cubic, rock salt structure consistent with NiO containing Co and Fe in a highly disordered state, possibly located at grain boundaries but likely alloyed into the NiO phase. While definitive conclusions about the relationship between the two phases could not be drawn, the authors proposed that superior activity of the high-Ce catalyst could be due to synergistic relationships between the two phases comprising the catalyst.

The effects of incorporating Co into $NiFeO_x$ has been reported in two very recent studies. Zhu *et al.* have investigated the performance of NiCoFe layered double hydroxides (LDH) by hydrothermal deposition of the metals onto a 3D conductive Ni foam (NF).[94] TEM analysis revealed that the NiCoFe LDH sheets have a lateral size of about 100 nm and are ultrathin. The OER activities of $Ni_{2.5}Co_{0.5}Fe$/NF and Ni_2CoFe/NF were compared to that of Ni_3Fe/NF by *iR*-corrected linear sweep voltammetry. For $Ni_{2.5}Co_{0.5}Fe$/NF the value of η_{OER} at a current density of 10 mA cm^{-2} is 275 mV and the Tafel slope is 99 mV per dec. By comparison, for Ni_3Fe/NF the value of η_{OER} is 305 mV and the Tafel slope is 92 mV per dec. The authors also found that the activation energy for the OER for $Ni_{2.5}Co_{0.5}Fe$/NF was 21 kJ mol^{-1}, whereas that for Ni_3Fe/NF was 52.3 kJ mol^{-1}. Based on their results, the authors proposed that Co improves the electrical conductivity of the catalyst and thereby contributes to the superior performance of $Ni_{2.5}Co_{0.5}Fe$/NF compared to Ni_3Fe/NF.

The structure and performance of NiCoFe layered triple hydroxides (LTHs) supported on carbon fiber cloth (CFC) for the electrochemical splitting of water have been investigated by Wang *et al.*[95] NiCoFe LTHs were electrodeposited onto the surface of CFC from a solution containing a mixture of Ni, Co, and Fe nitrates and well as ammonium nitrate. The HRTEM images show that the catalyst consists of thin, leaf-like sheets of LTHs organized on the surface of the CFC to form a very porous open structure. The OER activity of NiCoFe LTHs/CFC (Ni : Co : Fe = 8.7 : 10.5 : 1.0) was investigated in 1 M KOH by scanning voltammetry and compared with that of NiFe double hydroxides nano-sheet arrays (NiFe DHNAs/CFC) (Ni : Fe = 7.3 : 1). At a current density of 10 mA cm^{-2}, η_{OER} = 240 mV and the Tafel slope is 32 mV per dec for NiCoFe LTHs/CFC, whereas η_{OER} = 260 mV and the Tafel slope is 65 mV per dec for NiFe DHNAs/CFC. Another remarkable property of NiCoFe LTHs/CFC is its excellent stability. Only a 1% loss in the activity of this catalyst was observed when it was tested for 12 h in 1 M KOH at a current density of 20 mA cm^{-2}.

Improvements in the performance of $NiFeO_x$ catalysts by the incorporation of Mn have been reported by Lu *et al.*[96] Ternary NiFeMn layered double hydroxides were synthesized by dropwise addition of NaOH or Na_2CO_3 to an aqueous solution of Ni, Fe, and Mn nitrates. HRTEM images show that the catalyst consists of rag-like layers that are typically 50 nm wide and 3.7 nm thick. For an optimized composition of Ni : Fe : Mn = 3 : 1 : 0.5, the OER activity at 20 mA cm^{-2} is characterized by η_{OER} = 289 mV and a Tafel slope of

47 mV per dec. These characteristics compare favorably with those for a NiFe layered double hydroxide, for which $\eta_{OER} = 401$ mV and the Tafel slope is 65 mV per dec.

While most of the efforts aimed at improving the OER activity of $NiFeO_x$ have focused on the role of added cations, Hunter *et al.* have recently reported that the composition of the charge-compensating anions present in NiFe-layered double hydroxides ($[Ni_{1-x}Fe_x(OH)_2](A^{m-})_{x/m}$) also affect the OER activity.[97] $[Ni_3Fe(OH)_2](NO_3)$ was prepared by PLAL[58] and then ion-exchanged in a 1 M solution of BF_4^-, Cl^-, ClO_4^-, CO_3^{2-}, $C_2O_4^{2-}$, F^-, PO_4^{3-} or SO_4^{2-}. Electrochemical characterization of the $[Ni_3Fe(OH)_2](A^{m-})_{1/m}$ catalysts was carried out in a virtually CO_2-free 1 M solution of KOH, to avoid back exchange of the intercalated anion by CO_3^{2-}. Figure 3.12 illustrates the value of η_{OER} measured for a current density of 1 mA cm^{-2} as a function of the anion basicity characterized by the pK_a of the conjugate acid. A strong correlation is observed between the OER activity and the pK_a of the conjugate acid. The effect of the intercalated anion was stable over a period of 3 h in 1M KOH, suggesting that di- and tri-valent anions, in particular, outcompete OH^- anions for charge compensation between the LDH galleries. It was noted though, that if the KOH solution was exposed to air and allowed to absorb CO_2, carbonate anions formed, which rapidly displaced any anions having a lower conjugate acid pK_a. The authors suggest that the observed effect of anions may be due to a base-assisted deprotonation step during the OER. It is notable that no reference is made to the transformation of $[Ni_3Fe(OH)_2](A^{m-})_{1/m}$ to Ni_3FeOOH at a potential lower than that required for the onset of the OER. Therefore, it is conceivable that only a part of the $[Ni_3Fe(OH)_2](A^{m-})_{1/m}$ undergoes oxidation to Ni_3FeOOH and that, somehow, the unconverted part of the $[Ni_3Fe(OH)_2](A^{m-})_{1/m}$ influences the OER activity of Ni_3FeOOH.

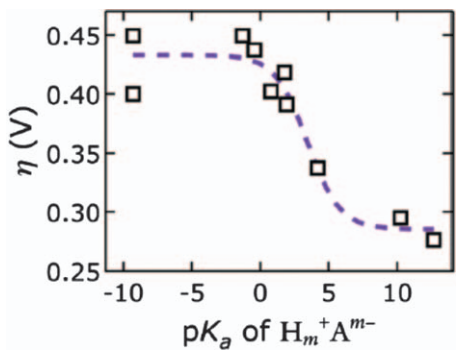

Figure 3.12 OER overpotential for $[Ni_3Fe(OH)_2](A^{m-})_{1/m}$ *versus* the pK_a of the conjugate acid of the anion A^{m-}. Experiment carried out at a current density of 1 mA cm^{-2} in virtually CO_2-free 1 M KOH.
Reproduced from ref. 97 with permission from the Royal Society of Chemistry.

3.9 Conclusions

Extensive research has established nickel iron oxyhydroxide, $Ni_{1-x}Fe_xOOH$, to be one of the most active catalysts for the OER. This material is attractive because it is based on earth-abundant elements and can operate without loss of activity under alkaline conditions. The OER activity of $Ni_{1-x}Fe_xOOH$ increases rapidly with x up to an Fe content of 12–25%, where it reaches a plateau, and then decreases with further addition of Fe. The highest OER activity is characterized by the lowest values for η_{OER} and β, and the lowest activation energy for the OER. Operando XAS studies of $Ni_{1-x}Fe_xOOH$ have shown that the initial increase in OER activity with added Fe is attributable to the substitution of Fe^{3+} cations for Ni^{3+} cations into the lattice of NiOOH. The substituted Fe^{3+} cations have an Fe–O bond length similar to that of Ni–O in NiOOH rather than the Fe–O bond distance in FeOOH, causing the electronic properties of such Fe^{3+} cations to be different from those in FeOOH. DFT calculations of the overpotential for the OER occurring on such Fe^{3+} cations show that it is significantly lower than that for Ni^{3+} sites in NiOOH, Fe^{3+} sites in FeOOH or Ni^{3+} sites in $Ni_{1-x}Fe_xOOH$, strongly suggesting that the superior OER activity of $Ni_{1-x}Fe_xOOH$ over NiOOH is due to the substituted Fe^{3+} cations. This conclusion is supported by scanning electrochemical microscopy measurement of the kinetics of the OER on Ni^{3+} and Fe^{3+} cations in NiOOH, FeOOH, and $Ni_{1-x}Fe_xOOH$. The decline in OER activity observed for Fe contents greater than the optimum is attributed to the formation of FeOOH, which has a much lower OER activity than $Ni_{1-x}Fe_xOOH$. While additives to NiOOH other than Fe have been explored, none of the bimetallic catalysts exhibit higher activity and stability than Fe. While even lower OER overpotentials and Tafel slopes than those observed for $Ni_{1-x}Fe_xOOH$ can be attained by the incorporation of Co or Mn, the means by which these additives have their effect is not understood.

A number of issues concerning the OER activity of $Ni_{1-x}Fe_xOOH$ remain outstanding and should be pursued. The first is the reason for the observed increase in the specific activity (turnover frequency) of Fe^{3+} cations with increasing Fe content. Closely related to this issue is the question of how does the local environment around Fe^{3+} cations affect the Tafel slope. The next issue would be to clearly establish the maximum extent to which Fe^{3+} cations can be substituted into the lattice of NiOOH and whether this level can be controlled through the synthetic strategy used to produce $Ni_{1-x}Fe_xOOH$. A third issue is the extent to which synthetic procedures can be devised to produce 3-D, highly porous $Ni_{1-x}Fe_xOOH$ layers that would enhance the superficial current density achievable for a given anode surface area.

Acknowledgements

The author acknowledges support from the Joint Center for Artificial Photosynthesis, a DOE Energy Innovation Hub, supported through the Office of Science of the U.S. Department of Energy under Award number DE-SC0004993.

References

1. N. S. Lewis and D. G. Nocera, Powering the planet: Chemical challenges in solar energy utilization, *Proc. Natl. Acad. Sci. U. S. A.*, 2006, **103**, 15729–15735.
2. H. B. Gray, Powering the plane with solar fuel, *Nat. Chem.*, 2009, **1**, 7.
3. A. Kudo and Y. Miseki, Heterogeneous photocatlayst materials for water splitting, *Chem. Soc. Rev.*, 2009, **38**, 253–278.
4. T. R. Cook, D. K. Dogutan, S. Y. Reece, Y. Surendranth, T. S. Teets and D. G. Nocera, Solar energy supply and storage for the legacy and non-legacy worlds, *Chem. Rev.*, 2010, **110**, 6474–6502.
5. B. M. Hunter, H. B. Gray and A. M. Müller, Earth-Abundant Heterogeneous Water Oxidation Catalysts, *Chem. Rev.*, 2016, DOI: 10.1021/acs.chem.rev.6b00398.
6. C. C. L. McCrory, S. Jung, J. C. Peters and T. F. Jaramillo, Benchmarking heterogeneous electrocatalysts for the oxygen evolution reaction, *J. Am. Chem. Soc.*, 2013, **135**, 16077–16987.
7. E. Fabbri, A. Habrederer, K. Waltar, R. Kotz and T. J. Schmidt, Development and perspective of oxide-based catalysts for the oxygen evolution reaction, *Catal. Sci. Technol.*, 2014, **4**, 3800–3821.
8. C. C. L. McCrory, S. Jung, I. M. Ferrer, S. M. Chatman, J. C. Peters and J. F. Jaramillo, Benchmarking Hydrogen Evolving and Oxygen Evolving Reaction Electocatalysts for Solar Water Splitting Devices, *J. Am. Chem. Soc.*, 2015, **137**, 4347–4357.
9. M. Gong and H. Dai, A mini review of NiFe-based materials as highly active oxygen evolution catalaysts, *Nano Res.*, 2015, **8**, 23–39.
10. O. Diaz-Morales, I. Ledezema-Yanez, M. T. M. Koper and F. Calle-Vallejo, Guidelines for the Rational Design of Ni-Based Double Hydroxide Electrocatalysts for the Oxygen Evolution Reaction, *ACS Catal.*, 2015, **5**, 5380–5387.
11. S. Jung, C. C. L. McCrory, I. M. Ferrer, J. C. Peters and T. F. Jaramillo, Benchmarking Nanoparticulate Metal Oxide Electrocatalysts for the Alkaline Water Oxidation Reaction, *J. Mater. Chem. A*, 2016, **4**, 3068–3076.
12. H. Bode, K. Dehmelt and J. Witte, Zur Kenntnis der Nickelhydroxidelektrode—I.Über Das Nickel (II)-Hydroxidhydrat, *Electrochim. Acta*, 1966, **11**, 1079–1087.
13. M. Cappadonia, J. Divisek, T. Vonderheyden and U. Stimming, Oxygen Evolution at Nickel Anodes in Concentrated Alkaline-Solution, *Electrochim. Acta*, 1994, **39**, 1559–1564.
14. P. W. T. Lu and S. Srinivasan, Electrochemical-Ellipsometric Studies of Oxide Film Formed on Nickel during Oxygen Evolution, *J. Electrochem. Soc.*, 1978, **125**, 1416–1422.
15. M. W. Louie and A. T. Bell, An Investigation of Thin-Film Ni-Fe Oxide Catalysts for the Electrochemical Evolution of Oxygen, *J. Am. Chem. Soc.*, 2013, **135**, 12329–12337.

16. B. S. Yeo and A. T. Bell, In Situ Raman Study of Nickel Oxide and Gold-Supported Nickel Oxide Catalysts for the Electrochemical Evolution of Oxygen, *J. Phys. Chem. C*, 2012, **116**, 8394–8400.
17. I. J. Godwin and M. E. G. Lyons, Enhanced Oxygen Evolution at Hydrous Nickel Oxide Electrodes via Electrochemical Ageing in Alkaline Solution, *Electrochem. Commun.*, 2013, **32**, 39–42.
18. M. Wehrens-Dijksma and P. H. L. Notten, Electrochemical Quartz Microbalance Characterization of Ni(OH)(2)-Based Thin Film Electrodes, *Electrochim. Acta*, 2006, **51**, 3609–3621.
19. D. A. Corrigan, The Catalysis of the Oxygen Evolution Reaction by Iron Impurities in Thin-Film Nickel-Oxide Electrodes, *J. Electrochem. Soc.*, 1987, **134**, 377–384.
20. X. H. Li, F. C. Walsh and D. Pletcher, Nickel Based Electrocatalysts for Oxygen Evolution in High Current Density, Alkaline Water Electrolysers, *Phys. Chem. Chem. Phys.*, 2011, **13**, 1162–1167.
21. R. N. Singh, J. P. Pandey and K. L. Anitha, Preparation of Electrodeposited Thin-Films of Nickel Iron-Alloys on Mild-Steel for Alkaline Water Electrolysis. 1. Studies on Oxygen Evolution, *Int. J. Hydrogen Energy*, 1993, **18**, 467–473.
22. L. Trotochaud, J. K. Ranney, K. N. Williams and S. W. Boettcher, Solution-Cast Metal Oxide Thin Film Electrocatalysts for Oxygen Evolution, *J. Am. Chem. Soc.*, 2012, **134**, 17253–17261.
23. M. Gong, Y. Li, H. Wang, Y. Liang, J. Z. Wu, J. Zhou, J. Wang, T. Regier, F. Wei and H. Dai, An Advanced Ni-Fe Layered Double Hydroxide Electrocatalyst for Water Oxidation, *J. Am. Chem. Soc.*, 2013, **135**, 8452–8455.
24. J. Landon, E. Demeter, N. Inoglu, C. Keturakis, I. E. Wachs, R. Vasic, A. I. Frenkel and J. R. Kitchin, Spectroscopic Characterization of Mixed Fe-Ni Oxide Electrocatalysts for the Oxygen Evolution Reaction in Alkaline Electrolytes, *ACS Catal.*, 2012, **2**, 1793–1801.
25. E. L. Miller and R. E. Rocheleau, Electrochemical Behavior of Reactively Sputtered Iron-Doped Nickel Oxide, *J. Electrochem. Soc.*, 1997, **144**, 3072–3077.
26. C. C. Hu and Y. R. Wu, Bipolar Performance of the Electroplated Iron-Nickel Deposits for Water Electrolysis, *Mater. Chem. Phys.*, 2003, **82**, 588–596.
27. R. D. L. Smith, M. S. Prevot, R. D. Fagan, Z. P. Zhang, P. A. Sedach, M. K. J. Siu, S. Trudel and C. P. Berlinguette, Photochemical Route for Accessing Amorphous Metal Oxide Materials for Water Oxidation Catalysis, *Science*, 2013, **340**, 60–63.
28. R. D. L. Smith, M. S. Prévot, R. D. Fagan, S. Trudel and C. P. Berlinguette, Water Oxidation Catalysis: Electrocatalytic Response to Metal Stoichiometry in Amorphous Metal Oxide Films Containing Iron, Cobalt, and Nickel, *J. Am. Chem. Soc.*, 2013, **135**, 11580–11586.
29. M. D. Merrill and R. C. Dougherty, Metal Oxide Catalysts for the Evolution of O_2 from H_2O, *J. Phys. Chem. C*, 2008, **112**, 3655–3666.

30. L. Trotochaud, S. L. Young, J. K. Ranney and S. W. Boettcher, Nickel-Iron Oxyhydroxide Oxygen-Evolution Electrocatalysts: The Role of Intentional and Incidental Iron Incorporation, *J. Am. Chem. Soc.*, 2014, **136**, 6744–6753.
31. S. Klaus, Y. Cai, M. W. Louie, L. Trotochaud and A. T. Bell, Effects of Fe Electrolyte Impurities on $Ni(OH)_2$/NiOOH Structure and Oxygen Evolution Activity, *J. Phys. Chem. C*, 2015, **119**, 7243–7254.
32. S. Klaus, M. W. Louie, L. Trotochaud and A. T. Bell, Role of Catalyst Preparation on the Electrocatalytic Activity of $Ni_{1-x}Fe_xOOH$ for the Oxygen Evolution Reaction, *J. Phys. Chem. C*, 2015, **119**, 18303–18316.
33. J. Swierk, S. Klaus, L. Trotochaud, A. T. Bell and T. D. Tilley, An Electrochemical Study of the Energetics of the Oxygen Evolution Reaction at Nickel Iron (oxy)hydroxide Catalysts, *J. Phys. Chem. C*, 2015, **119**, 19022–19029.
34. D. Friebel, M. W. Louie, M. Abjdich, K. E. Sewald, Y. Cai, A. M. Wise, M.-J. Cheng, D. Sokaras, T.-C. Weng, R. Alonso, R. C. Davis, J. R. Bargar, J. K. Norskov, A. Nilsson and A. T. Bell, Identification of Highly active Fe Sites in (Ni,Fe)OOH for Electrocatalytic Splitting of Water, *J. Am. Chem. Soc.*, 2015, **137**, 1305–1313.
35. W. M. Heijboer, P. Glatzel, K. R. Sawant, R. F. Lobo, U. Bergmann, R. A. Barrea, D. C. Koningsberger, B. M. Weckhuysen and F. M. F. de Groot, Kβ-Detected XANES of Framework-Substituted FeZSM-5 Zeolites, *J. Phys. Chem. B*, 2004, **108**, 10002–10011.
36. T. E. Westre, P. Kennepohl, J. G. DeWitt, B. Hedman, K. O. Hodgson and E. I. Solomon, A Multiplet Analysis of Fe K-Edge $1s \rightarrow 3d$ Pre-Edge Features of Iron Complexes, *J. Am. Chem. Soc.*, 1997, **119**, 6297–6314.
37. D. K. Bediako, B. Lassalle-Kaiser, Y. Surendranath, J. Yano, V. K. Yachandra and D. G. Nocera, Structure–Activity Correlations in a Nickel–Borate Oxygen Evolution Catalyst, *J. Am. Chem. Soc.*, 2012, **134**, 6801–6809.
38. M. Balasubramanian, C. A. Melendres and S. Mini, X-ray Absorption Spectroscopy Studies of the Local Atomic and Electronic Structure of Iron Incorporated into Electrodeposited Hydrous Nickel Oxide Films, *J. Phys. Chem. B*, 2000, **104**, 4300–4306.
39. T. W. Capehart, D. A. Corrigan, R. S. Conell, K. I. Pandya and R. W. Hoffman, In situ extended x-ray absorption fine structure spectroscopy of thin-film nickel hydroxide electrodes, *Appl. Phys. Lett.*, 1991, **58**, 865–867.
40. A. N. Mansour and C. A. Melendres, XAFS investigation of the structure and valency of nickel in some oxycompounds, *Phys. B Condens. Matter*, 1995, **208–209**, 583–584.
41. Y. Hu, I. T. Bae, Y. Mo, D. A. Scherson and M. R. Antonio, In situ X-ray absorption fine structure and optical reflectance studies of electrodeposited nickel hydrous oxide films in alkaline electrolytes, *Can. J. Chem.*, 1997, **75**, 1721–1729.

42. M. Morishita, S. Ochiai, T. Kakeya, T. Ozaki, Y. Kawabe, M. Watada, S. Tanase and T. Sakai, Phase Transformation in the Charge-Discharge Process and the Structural Analysis by Synchrotron XAFS and XRD for Nickel Hydroxide Electrode, *Electrochem*, 2008, **76**, 802.
43. X. Yang, K. Takada, M. Itose, Y. Ebina, R. Ma, K. Fukuda and T. Sasaki, Highly Swollen Layered Nickel Oxide with a Trilayer Hydrate Structure, *Chem. Mater.*, 2008, **20**, 479–485.
44. A. Bianconi; J. Garcia and M. Benfatto, XANES in condensed systems, in *Synchrotron Radiation in Chemistry and Biology I; Topics in Current Chemistry*, Springer, Berlin Heidelberg, 1988, pp. 29–67.
45. J. Stöhr, F. Sette and A. L. Johnson, Near-Edge X-Ray-Absorption Fine-Structure Studies of Chemisorbed Hydrocarbons: Bond Lengths with a Ruler, *Phys. Rev. Lett.*, 1984, **53**, 1684–1687.
46. L. Guerlou-Demourgues, L. Fournès and C. Delmas, In Situ ^{57}Fe Mössbauer Spectroscopy Study of the Electrochemical Behavior of an Iron-Substituted Nickel Hydroxide Electrode, *J. Electrochem. Soc.*, 1996, **143**, 3083–3088.
47. M. Görlin, P. Chernev, J. Ferreira de Araújo, T. Reier, S. Dresp, B. Paul, R. Kränhert, H. Dau and P. Strasser, Oxygen Evolution Reaction Dynamics, Faradic Charge Efficiency, and the Active Metal Redox States of Ni-Fe Oxide Water Splitting Electorcatalysts, *J. Am. Chem. Soc.*, 2016, **138**, 5603–5614.
48. J. K. Nørskov, J. Rossmeisl, A. Logadottir, L. Lindqvist, J. R. Kitchin, T. Bligaard and H. Jónsson, Origin of the Overpotential for Oxygen Reduction at a Fuel-Cell Cathode, *J Phys Chem B*, 2004, **108**, 17886–17892.
49. I. C. Man, H. Su, F. Calle-Vallejo, H. A. Hansen, J. I. Martínez, N. G. Inoglu, J. Kitchin, T. F. Jaramillo, J. K. Nørskov and J. Rossmeisl, Universality in Oxygen Evolution Electrocatalysis on Oxide Surfaces, *ChemCatChem*, 2011, **3**, 1159–1165.
50. M. T. M. Koper, Thermodynamic theory of multi-electron transfer reactions: Implications for electrocatalysis, *J. Electroanal. Chem.*, 2011, **660**, 254–260.
51. P. Liao, J. A. Keith and E. A. Carter, Water oxidation on pure and doped hematite (0001) surfaces: prediction of Co and Ni as effective dopants for electrocatalysis, *J. Am. Chem. Soc.*, 2012, **134**, 13296–13309.
52. Y.-F. Li and A. Selloni, Mechanism and Activity of Water Oxidation on Selected Surfaces of Pure and Fe-Doped NiO_x, *ACS Catal.*, 2014, 1148–1153.
53. H. S. Ahn and A. J. Bard, Surface Interrogation Scanning Electrochemical Microscopy of $Ni_{1-x}Fe_xOOH$ $(0<x<0.27)$ Oxygen-Evolving Catalyst: Kinetics of the ''Fast'' Iron Sites, *J. Am. Chem. Soc.*, 2016, **119**, 8147–8154.
54. J. Y. C. Chen, L. Dang, H. Liang, W. Bi, J. B. Gerken, S. Jin, A. A. Alp and S. S. Stahl, Operando Analysis of NiFe and Fe Oxyhydroxide Electrocatalysts for Water Oxidation: Detection of Fe^{4+} by Mossbauer Spectroscopy, *J. Am. Chem. Soc.*, 2015, **137**, 15090–15093.

55. J. Landon, E. Demeter, N. Đnoğlu, C. Keturakis, I. E. Wachs, R. Vasić, A. I. Frenkel and J. R. Kitchin, Spectroscopic Characterization of Mixed Fe–Ni Oxide Electrocatalysts for the Oxygen Evolution Reaction in Alkaline Electrolytes, *ACS Catal.*, 2012, **2**, 1793–1801.
56. M. Gong, Y. Li, H. Wang, Y. Liang, J. Z. Wu, J. Zhou, J. Wang, T. Regier, F. Wei and H. Dai, An advanced Ni–Fe layered double hydroxide electrocatalyst for water oxidation, *J. Am. Chem. Soc.*, 2013, **135**, 8452–8455.
57. J. B. Gerken, S. E. Shaner, R. C. Massé, N. J. Porubsky and S. S. Stahl, A survey of diverse earth abundant oxygen evolution electrocatalysts showing enhanced activity from Ni–Fe oxides containing a third metal, *Energy Environ. Sci.*, 2014, **7**, 2376–2382.
58. B. M. Hunter, J. D. Blakemore, M. Deimund, H. B. Gray, J. R. Winkler and A. M. Muller, Highly active mixed-metal nanosheet water oxidation catalysts made by pulsed-laser ablation in liquids, *J. Am. Chem. Soc.*, 2014, **136**, 13118–13121.
59. K. L. Nardi, N. Yang, C. F. Dickens, A. L. Strickler and S. F. Bent, Creating Highly Active Atomic Layer Deposited NiO Electrocatalysts for the Oxygen Evolution Reaction, *Adv. Energy Mater.*, 2015, **5**, 1500412.
60. J. A. Bau, E. J. Luber and J. M. Buriak, Oxygen Evolution Catalyzed by Nickel-Iron Oxide Nanocrystals with a Nonequilibrium Phase, *ACS Appl. Mater. Interfaces*, 2015, **7**, 19755–19763.
61. J. Qi, W. Zhang, R. Xiang, K. Liu, H.-Y. Wang, M. Chen, Y. Han and R. Cao, Porous Nickel-Iron Oxide as a Highly Efficient Electrocatalyst for Oxygen Evolution Reaction, *Adv. Sci.*, 2015, **2**, 1500199.
62. X. Lu and C. Zhao, Electrodeposition of hierarchically structured three-dimensional nickel iron electrodes for efficient oxygen evolution at high current densities, *Nat. Commun.*, 2015, **6**, 6616.
63. Y. Feng, H. Zhang, Y. Zhang, X. Li and Y. Wang, Ultrathin Two-Dimensional Free-Standing Sandwiched NiFe/C for High-Efficiency Oxygen Evolution Reaction, *ACS Appl. Mater. Interfaces*, 2015, **7**, 9203–9210.
64. L. Zhiyi, L. Yingjie, L. Xiaodong, J. Liu and X. Sun, Nanoarray based ''superaerophobic'' surfaces for gas evolution reaction electrodes, *Mater. Horiz.*, 2015, **2**, 294.
65. X. Yan, L. Tian, K. Li, S. Atkins, H. Zhao, J. Murowchick, L. Liu and X. Chen, $FeNi_3$/NiFeOxNanohybrids as Highly Efficient Bifunctional Electrocatalysts for Overall Water Splitting, *Adv. Mater. Interfaces*, 2016, 1600368.
66. Z. Li, M. Shao, H. An, Z. Wang, S. Xu, M. Wei, D. G. Evans and X. Duan, Fast electrosynthesis of Fe-containing layered double hydroxide arrays toward highly efficient electrocatalytic oxidation reactions, *Chem. Sci.*, 2015, **6**, 6624–6631.
67. X. Cui, P. Ren, D. Deng, J. Deng and X. Bao, Single layer graphene encapsulating nonprecious metals as high-performance electrocatalysts for water oxidation, *Energy Environ. Sci.*, 2016, **9**, 123–129.

68. B. M. Hunter, W. Hieringer, J. R. Winkler, H. B. Gray and A. M. Müller, Effect of interlayer anions on [NiFe]-LDH nanosheet water oxidation activity, *Energy Environ. Sci.*, 2016, **9**, 1734–1743.
69. Y. Feng, H. Zhang, L. Fang, Y. Mu and Y. Wang, Uniquely Monodispersing NiFe Alloyed Nanoparticles in Three-Dimensional Strongly Linked Sandwiched Graphitized Carbon Sheets for High-Efficiency Oxygen Evolution Reaction, *ACS Catal.*, 2016, **6**, 4477–4485.
70. A. Sivanantham, P. Ganesan and S. Shanmugam, Hierarchical $NiCo_2S_4$ Nanowire Arrays Supported on Ni Foam: An Efficient and Durable Bifunctional Electrocatalyst for Oxygen and Hydrogen Evolution Reactions, *Adv. Funct. Mater.*, 2016, **26**, 4661–4672.
71. C. Xiao, Y. Li, X. Lu and C. Zhao, Bifunctional Porous NiFe/$NiCo_2O_4$/Ni Foam Electrodes with Triple Hierarchy and Double Synergies for Efficient Whole Cell Water Splitting, *Adv. Funct. Mater.*, 2016, **26**, 3515–3523.
72. F. Rong, J. Zhao, Q. Yang and C. Li, Nanostructured hybrid NiFeOOH/CNT electrocatalysts for oxygen evolution reaction with low overpotential, *RSC Adv.*, 2016, **6**, 74536–74544.
73. W. Xu, Z. Lu, P. Wan, Y. Kuang and X. Sun, High-Performance Water Electrolysis System with Double Nanostructured Superaerophobic Electrodes, *Small*, 2016, **12**, 2492–2498.
74. F. Dionigi and P. Strasser, NiFe-Based (Oxy)hydroxide Catalysts for Oxygen Evolution Reaction in Non-Acidic Electrolytes, *Adv. Energy Mater.*, 2016, 1600621.
75. T. T. H. Hoang and A. A. Gewirth, High Activity Oxygen Evolution Reaction Catalysts from Additive-Controlled Electrodeposited Ni and NiFe Films, *ACS Catal.*, 2016, **6**, 1159–1164.
76. C. G. Morales-Guio, L. Liardet and X. Hu, Oxidatively Electrodeposited Thin-Film Transition Metal (Oxy)hydroxides as Oxygen Evolution Catalysts, *J. Am. Chem. Soc.*, 2016, **138**, 8946–8957.
77. Y. Q. Gao, X. Y. Liu and G. W. Yang, Amorphous mixed-metal hydroxide nanostructures for advanced water oxidation catalysts, *Nanoscale*, 2016, **8**, 5015–5023.
78. K. Zhu, M. Li, X. Li, X. Zhu, J. Wang and W. Yang, Enhancement of oxygen evolution performance through synergetic action between NiFe metal core and NiFeOx shell, *Chem. Commun.*, 2016, DOI: 10.1039/c6cc04951f.
79. J. Newman and K. E. Thomas-Alyea, *Electrochemical Systems*, Wiley, New York, 3rd edn, 2004.
80. (a) M. E. G. Lyons and M. P. Bradon, The oxygen evolution reaction on passive oxide covered transition metal electrodes in aqueous alkaline solution. Part 1-Nickel, *Int. J. Electrochem Soc.*, 2008, **3**, 1386–1424; (b) M. E. G. Lyons and M. P. Bradon, The oxygen evolution reaction on passive oxide covered transition metal electrodes in aqueous alkaline solution. Part 1-Nickel. The Oxygen Evolution Reaction on Passive Oxide Covered Transition Metal Electrodes in Alkaline Solution. Part III-Iron, *Int. J. Electrochem Soc.*, 2008, **3**, 1463–1503.

81. Y. Matsumoto and E. Sato, Electrocatalytic properties of transition-metal oxides for oxygen evolution reaction, *Mater. Chem. Phys.*, 1986, **14**, 397–426.
82. Y. Ping, R. J. Nielsen and W. A. Goddard, The Reaction Mechanism with Free Energy Barrriers at Constant Potential for the Oxygen Evolution Reaction at the IrO_2 (110) surface, *J. Am. Chem. Soc.*, 2016, DOI: 10.1021/jacs.6b07557.
83. D. A. Corrigan and R. M. Bendert, Effect of coprecipitated metal ions on the electrochemistry of nickel hydroxide thin films: cyclic voltammetry in 1M KOH, *J. Electrochem. Soc.*, 1989, **136**, 723–728.
84. S. I. Cordoba, R. E. Carbonia and M. L. Teijelo, The electrochemical response of binary mixtures of hydrous transition metal hydroxides co-precipitated on conducting substrates with reference to the oxygen evolution reaction, *Electrochim. Acta*, 1986, **31**, 1321–1332.
85. P. W. T. Lu and S. Srinivasan, Nickel-Based Alloys as Electrocatalysts for Oxygen Evolution from Alkaline Solutions, *J. Electrochem. Soc.*, 1978, **125**, 265–270.
86. L. Qian, Z. Lu, T. Xu, X. Wu, Y. Tian, Y. Li, Z. Huo, X. Sun and X. Duan, Trinary Double Hydroxides as High-Performance Bifunctional Materials for Oxgen Electrocatalysis, *Adv. Energy Mater.*, 2015, **5**, 1500245.
87. K.-Y. Niu, F. Lin, S. Jung, L. Fang, D. Nordlund, C. C. L. McCrory, T.-C. Weng, P. Ercius, M. M. Doeff and H. Zheng, Tuning Complex Transition Metal Hydroxide Nanostructures as Active Catalysts for Water Oxidation by a Laser–Chemical Route, *Nano Lett.*, 2015, **15**, 2498–2503.
88. L. J. Enman, M. L. Burke, A. S. Batchellor and S. W. Boettcher, Effects of Intentionally Incorporated Metal Cations on the Oxygen Evolution Electorcatalytic Activity of Nickel (Oxy)hydroxide in Alkaline Media, *ACS Catal.*, 2015, **6**, 2416–2423.
89. J. B. Gerken, J. Y. C. Chen, R. C. Masse, A. B. Powell and S. S. Stahl, Development of O_2-senstitive fuorescence-qunenching assay for the combinatorial discovery of electrocatalysts for water oxidation, *Angew. Chem. Inter. Ed.*, 2012, **51**, 6676–6680.
90. J. B. Gerken, S. E. Shanner, R. C. Masse, N. J. Porbusky and S. S. Stahl, A survey of diverse earth abundant oxygen evolution electrocatalysts showing enhanced activity from Ni-Fe oxides containing a third element, Energy Environ. S*ci.*, 2014, **7**, 2376–2382.
91. J. A. Haber, Y. Cai, S. Jung, C. Xiang, S. Mitrovic, J. Jin, A. T. Bell and J. M. Gregoire, Discovering Ce-rich oxygen evolution catalysts from high throughput screening to water electrolysis, *Energy Environ. Sci.*, 2014, **7**, 682–688.
92. J. A. Haber, C. C. Xiang, D. Gueverra, S. H. Jung, J. Jin and J. M. Gregoire, High-throughput mapping of the electrochemical properties of (Ni-Fe-Co-Ce)O_x oxygen-evolving catalysts, *ChemElectroChem*, 2014, **1**, 524–528.
93. J. A. Haber, E. Anzenburg, J. Yano, C. Kisielowski and J. M. Gregoire, Multiphase Nanostructure of a Quinary Metal Oxide Electrocatalyst

Reveals a New Direction for OER Electrocatalyst Design, *Adv. Energy Mater.*, 2015, **5**, 1402307.

94. X. Zhu, C. Tang, H.-F. Wang, B.-Q. Li, Q. Zhang, C. Li, C. Yang and F. Wei, Monolithic-structured ternary hydroxides as freestanding bifunctional electrocatalysts for overall water splitting, *J. Mater. Chem. A.*, 2016, **4**, 7245–7250.
95. A.-L. Wang, H. Xu and G.-R. Li, NiCoFe Layered Triple Hydroxides with Porous Structures as High-Performance Electrocatalysts for Overall Water Splitting, *ACS Energy Lett.*, 2016, **1**, 445–453.
96. Z. Lu, L. Qian, Y. Tian, Y. Li, X. Sun and X. Duan, Ternary NiFeMn layered double hydroxides as highly-efficient oxygen evolution catalysts, *Chem. Commun.*, 2016, **52**, 908–911.
97. B. M. Hunter, W. Hieringer, J. R. Winkler, H. B. Gray and A. M. Muller, Effect of interlayer anions on [NiFe]-LDH nonsheet water oxidation activity, *Energy Environ. Sci.*, 2016, **9**, 1734–1743.